

## Empirical Model of 10–130 MeV Solar Energetic Particle Spectra at 1 AU Based on Coronal Mass Ejection Speed and Direction

Alessandro Bruno<sup>1,2</sup>  ·  
Ian G. Richardson<sup>1,3</sup> 

© Springer ●●●●

**Abstract** We present a new empirical model to predict solar energetic particle (SEP) event-integrated and peak intensity spectra between 10 and 130 MeV at 1 AU, based on multi-point spacecraft measurements from the *Solar TERrestrial Relations Observatory* (STEREO), the *Geostationary Operational Environmental Satellites* (GOES), and the *Payload for Antimatter Matter Exploration and Light-nuclei Astrophysics* (PAMELA) satellite experiment. The analyzed data sample includes 32 SEP events occurring between 2010 and 2014, with a statistically significant proton signal at energies in excess of a few tens of MeV, unambiguously recorded at three spacecraft locations. The spatial distributions of SEP intensities are reconstructed by assuming an energy-dependent 2D Gaussian functional form, and accounting for the correlation between the intensity and the speed of the parent coronal mass ejection (CME), and the magnetic-field-line connection angle. The CME measurements used are from the Space Weather Database Of Notifications, Knowledge, Information (DONKI). The model performance, including its extrapolations to lower/higher energies, is tested by comparing with the spectra of 20 SEP events not used to derive the model parameters. Despite the simplicity of the model, the observed and predicted event-integrated and peak intensities at Earth and at the STEREO spacecraft for these events show remarkable agreement, both in the spectral shapes and their absolute values.

---

A. Bruno  
[alessandro.bruno-1@nasa.gov](mailto:alessandro.bruno-1@nasa.gov)

I.G. Richardson  
[ian.g.richardson@nasa.gov](mailto:ian.g.richardson@nasa.gov)

<sup>1</sup> Heliophysics Division, NASA Goddard Space Flight Center, Greenbelt, MD, USA

<sup>2</sup> Department of Physics, Catholic University of America, Washington DC, USA

<sup>3</sup> Department of Astronomy, University of Maryland, College Park, MD, USA

**Keywords:** Solar energetic particles; coronal mass ejections; spacecraft missions; space weather

## 1. Introduction

Solar energetic particle (SEP) events are major space-weather disturbances both in the heliosphere and in the near-Earth environment, which significantly constrain human activities in space by posing serious radiation hazards for satellites, avionics, astronauts, and aircraft passengers on polar routes (e.g. Shea and Smart, 2012). Modern society’s vulnerability to space-weather effects is exacerbated by its increasing reliance on technological systems (e.g. Eastwood et al., 2017). Predicting SEP event occurrence and impact is therefore of crucial importance, especially in view of planned long-duration missions to the Moon and to Mars, beyond the Earth’s protective atmosphere and magnetosphere (e.g. Cucinotta et al., 2010).

Large SEP events of space-weather interest are believed to be primarily accelerated by coronal mass ejection (CME)-driven shocks (e.g. Desai and Giacalone, 2016). The acceleration efficiency is predicted to depend on several concomitant factors, including the shock speed, geometry, and age (e.g. Tylka et al., 2005; Zank, Li, and Verkhoglyadova, 2007), the coronal magnetic-field strength and configuration (e.g. Kong et al., 2017, 2019), the presence of seed-particle populations (e.g. Kahler, Reames, and Burkepile, 2000; Kahler, 2001; Tylka et al., 2005; Cliver, 2006; Desai et al., 2006, 2016) and pre-existing turbulence (e.g. Gopalswamy, Yashiro, and Krucker, 2004; Li et al., 2012; Ding et al., 2013; Zhao and Li, 2014). Although they might be included in a full physics-based SEP prediction model, most of these factors are difficult to evaluate or are not currently measurable directly. A number of authors have reported a significant correlation between SEP event intensities and the parent CME speeds, which has been interpreted as evidence that SEPs are accelerated by shocks (e.g. Cane, Richardson, and von Rosenvinge, 2010; Gopalswamy et al., 2002; Gopalswamy, Yashiro, and Krucker, 2004; Kahler, Hildner, and Van Hollebeke, 1978; Kahler et al., 1984, 1987; Kahler and Vourlidas, 2005; Lario and Karelitz, 2014; Reames, 2000; Richardson et al., 2014; Richardson, von Rosenvinge, and Cane, 2015). In particular, the most energetic SEP events, such as those causing the so-called ground-level enhancements (GLEs), were found to be typically associated with the fastest ( $\approx 2000 \text{ km s}^{-1}$  average velocity) CMEs (Gopalswamy et al., 2005). Such observations suggest that the CME velocity might be used as a proxy for the shock-acceleration efficiency in an empirical SEP prediction model.

Another important factor determining the relative particle intensity during an SEP event – as well as the occurrence of GLEs – is the connection angle, defined as the angular distance between the SEP source at the Sun and the footpoint of the interplanetary magnetic-field (IMF) line passing the observing spacecraft. As a number of studies have shown, measured particle intensities tend to decrease with increasing connection angle (e.g. Van Hollebeke, Ma Sung, and McDonald, 1975; Kallenrode, 1993; Lario et al., 2006, 2013; Richardson et al., 2014; Richardson, von Rosenvinge, and Cane, 2017; Gopalswamy et al.,

2014). In addition, Cane, Reames, and von Rosenvinge (1988) demonstrated that the longitudinal distribution of SEPs and its energy dependence, is also determined by the connection to the CME-driven shock. Since its launch in 2006, the *Solar TErrestrial RElations Observatory* (STEREO) mission (Kaiser et al., 2008) has enabled, in combination with near-Earth measurements, a multi-point investigation of SEP events over a wide longitudinal range with minimal radial gradient effects (e.g. Lario et al., 2013; Richardson et al., 2014; Richardson, von Rosenvinge, and Cane, 2017; Cohen, Mason, and Mewaldt, 2017). However, the limited number of observation points have precluded any precise measurement of the longitudinal distribution, which has been usually assumed to be Gaussian in connection angle following Lario et al. (2006).

Richardson et al. (2014) discussed the properties of all the  $>25$  MeV proton events observed by the STEREO spacecraft and/or at Earth during 2006–2013 and summarized the intensity of 14–24 MeV protons in 25 SEP three-spacecraft events as

$$\Phi(\beta) \approx 0.013 \exp(0.0036 V_{\text{cme}} - \beta^2/2\sigma_{\text{sep}}^2), \quad (1)$$

where  $\Phi$  [in  $\text{MeV}^{-1}\text{sr}^{-1}\text{s}^{-1}\text{cm}^{-2}$ ] is the peak intensity of the Gaussian fit to the event,  $V_{\text{cme}}$  [in  $\text{kms}^{-1}$ ] is the speed of the related CME,  $\beta$  is the longitudinal connection angle and  $\sigma_{\text{sep}} = 43^\circ$  is the mean Gaussian standard deviation for these events. Richardson, Mays, and Thompson (2018) used the relationship in Equation 1 to develop an empirical model (subsequently named “SEPSTER” – SEP predictions based on STEREO observations) to predict the 14–24 MeV proton peak intensity based on CME speed and direction relative to the observing spacecraft. The spatial width value [ $\sigma_{\text{sep}}$ ] derived by Richardson et al. (2014) is consistent with the results obtained by Lario et al. (2013) and Paassilta et al. (2018) using the 25–53 MeV and the  $>55$  MeV proton peak intensities, respectively. Cohen, Mason, and Mewaldt (2017) analyzed the 0.3, 1, and 10  $\text{MeV n}^{-1}$  event-integrated intensities of H, He, O, and Fe ions, reporting a mean  $\sigma_{\text{sep}}$  value decreasing from  $\approx 52^\circ$  to  $\approx 36^\circ$  with increasing energy, which they suggested is in line with theoretical expectations that higher-energy particles are efficiently accelerated over a smaller shock region around the “nose” or for shorter times as the shock expands (e.g. Lee, 2005; Caprioli and Spitkovsky, 2014; Dalla, Marsh, and Battarbee, 2017), or are less affected by field-line co-rotation effects (e.g. Giacalone and Jokipii, 2012).

Although typically neglected when compared to longitude-related effects, the SEP intensities at a given location are also affected by the latitudinal magnetic connectivity to the source (Dalla and Aguada, 2010; Gopalswamy and Mäkelä, 2014). The latitude influence might be expected to become more important for higher-energy particles if they are accelerated by the strongest regions of a shock close to the nose or, in an alternative scenario, by the associated solar flare. Consistent with this prediction, Gopalswamy et al. (2013, 2014) showed that the latitudinal distance from the Ecliptic is typically larger for energetic eruptions not associated with GLE events, suggesting that the poorer connection to Earth was responsible. Although a direct estimate of the SEP event latitudinal spread was previously investigated in the pre-STEREO era by the *Ulysses* mission (see,

e.g., Struminsky et al., 2006 and references therein), no similar observations are currently available.

Recently, de Nolfo et al. (2019) derived the  $>80$  MeV proton spatial distribution of 14 events by means of a 2D Gaussian modeling accounting for both longitudinal and latitudinal connectivity, based on the assumption of a spherical symmetry of particle intensities. In the present work, following Richardson et al. (2014) and Richardson, Mays, and Thompson (2018), we exploit the widely reported correlation between particle intensities and CME speeds, as well as the spatial distribution reconstructed for a number of SEP events with the 2D approach of de Nolfo et al. (2019), to develop an empirical model that predicts 10–130 MeV proton spectra at 1 AU. The article is structured as follows: in Section 2 we present the SEP events used to train the model, along with the spectral analysis of measured intensities. In Sections 3 and 4 we describe the method for the reconstruction of the SEP spatial distribution, and the algorithm based on the CME speed and direction. In Sections 5 and 6 we discuss the model uncertainties and test its performance. Finally, Section 7 summarizes the study and presents our conclusions.

## 2. Data Analysis

### 2.1. Data Sample

The starting point for developing the empirical SEP prediction formula is a set of 32 SEP events occurring between 2010 and 2014, in which proton intensities above a few tens of MeV were unambiguously measured at three 1 AU locations by the twin STEREO spacecraft and near-Earth assets, including the *Geostationary Operational Environmental Satellites* (GOES) and the *Antimatter Matter Exploration and Light-nuclei Astrophysics* (PAMELA) experiment onboard the *Resurs-DK1* Russian satellite (e.g. Adriani et al., 2017). The selected period corresponds to the interval when all of these spacecraft were operating and numerous SEP events were detected at Earth and the STEREO locations (e.g. Richardson et al., 2014; Paassilta et al., 2018), around the maximum of Solar Cycle 24.

The relevant parameters associated with the parent eruptions are reported in Table 1. The first column gives the event number. Columns 2–5 list the CME first appearance time [UT], space (3D) speed, width and direction in Stonyhurst heliographic (HGS) coordinates from the Space Weather Database Of Notifications, Knowledge, Information (DONKI) developed at the Community Coordinated Modeling Center (CCMC). These are based on the triangulation of the STEREO and the *Solar and Heliospheric Observatory* (SOHO) coronagraph measurements at a  $\approx 21.5$  solar radii ( $R_{\odot}$ ) height (Liu et al., 2010; Mays et al., 2015). The CME parameters are not available for events #1 and #20; the resulting sample includes CMEs with speeds ranging from 650 to 3454 km s<sup>-1</sup>. We choose to use CME parameters from DONKI because, in addition to being based on multi-point coronagraph observations, if available, these parameters include

**Table 1.** CMEs associated with the SEP events analyzed in this work. The first column is the event number. Columns 2–5 report the CME first appearance time [UT], space speed [km s<sup>-1</sup>], angular width [°] and direction from the DONKI catalog. The CME parameters are not available for events #1 and #20. The right three columns list the location of the footpoints of the Parker spiral field lines crossed by each spacecraft (STEREO-A/B and GOES/PAMELA) at CME onset, mapped ballistically back to 2.5 R<sub>⊙</sub>. Footpoints locations and CME directions are expressed in terms of HGS latitudes/longitudes.

#	Onset time	CME			Spacecraft footpoints		
		Speed	Width	Direction	STB	Earth	STA
1	2010-06-12T?	...	...	...	S06E07	N00W58	N07W116
2	2010-08-14T10:12	950	80	N11W58	N00W00	N06W60	N04W141
3	2010-08-18T06:00	1091	80	S30W97	N00W08	N06W63	N03W139
4	2010-09-08T23:26	850	90	N08W96	N02W00	N07W55	N00W133
5*	2011-03-21T02:54	1000	140	N20W130	S00E29	S07W67	N01W139
6	2011-08-04T04:10	1950	120	N14W40	S03E45	N05W64	N02W154
7*	2011-09-06T22:40	650	60	N20W20	S00E43	N07W57	S01W174
8	2011-09-22T11:24	1000	140	N10E90	N01E39	N07W62	S03W161
9	2011-10-22T11:20	990	110	N52W90	N04E37	N05W72	S06E178
10*	2011-11-03T22:39	1100	130	S07E160	N05E22	N04W64	S06E173
11	2011-11-26T07:12	930	144	N23W45	N06E46	N01W57	S07W160
12*	2012-01-23T04:00	2211	124	N41W26	N06E46	S05W58	S02W173
13*	2012-03-07T00:36	2200	100	N30E60	N03E53	S07W62	N02W169
14*	2012-05-17T01:48	1500	90	S10W75	S04E58	S02W62	N07W162
15	2012-05-26T22:54	1100	140	N05W110	S05E81	S01W58	N07W173
16*	2012-07-23T02:36	3435	160	S15W144	S06E44	N05W50	N01W163
17	2012-08-31T20:36	1498	150	S15E63	S03E37	N07W63	S03E178
18	2013-02-06T00:36	1226	76	N30E35	N07E49	S06W66	N01E153
19*	2013-04-11T07:36	675	116	N00E15	N02E66	S05W66	N07W177
20	2013-04-24T?	...	...	...	N00E78	S04W70	N07W177
21	2013-05-13T16:18	1900	80	N10E70	S01E81	S01W60	N03W175
22*	2013-05-22T13:24	1200	120	N10W80	S02E92	S00W47	N04E170
23	2013-06-21T03:24	1970	140	S19E57	S05E100	N00W44	N04E172
24	2013-08-19T23:12	1200	90	N17W180	S08E72	N02W48	N02E165
25	2013-10-25T15:12	980	80	N15E63	S03E60	N03W67	S02E173
26*	2013-11-02T04:48	1078	150	N05W145	S00E90	N02W62	S02E162
27	2013-11-19T10:39	910	100	S29W82	N01E78	N01W54	S03E143
28	2013-12-26T03:40	1600	180	S31E134	N05E92	S01W75	S03E160
29*	2014-01-06T08:09	1275	90	S03W102	N05E92	S01W51	S02E150
30*	2014-01-07T18:24	2061	98	S24W30	N06E77	S01W52	S02E152
31*	2014-02-25T01:25	1670	132	S11E78	N03E119	S02W48	S00E149
32*	2014-09-01T11:24	1700	92	N01E155	S05E106	N02W46	S01E138

\*Associated with SEP events observed by PAMELA (Bruno et al., 2018).

the CME direction which is not provided by most other CME catalogs. Furthermore, DONKI includes reports of observations of space-weather phenomena and their interpretation in real-time provided by the CCMC space-weather team, and hence it simulates how a CME-based SEP prediction scheme might be applied in a forecasting environment. Finally, columns 6–8 show the HGS coordinates of

the magnetic footpoints of the IMF lines passing through STEREO-B, the Earth, and STEREO-A, estimated at CME first appearance time and at a  $2.5 R_{\odot}$  radial distance – the nominal “source surface” height – based on a simple IMF spiral model, as described in Appendix A.

## 2.2. SEP Spectral Analysis

Our multi-spacecraft analysis of SEP events is based on the proton intensities measured by the *Solar Electron and Proton Telescope* (SEPT; Müller-Mellin et al., 2008), the *Low Energy Telescope* (LET; Mewaldt et al., 2008), and the *High Energy Telescope* (HET; von Rosenvinge et al., 2008) onboard the twin STEREOs, and by the *Energetic Proton, Electron, and Alpha Detector* (EPEAD) and the *High Energy Proton and Alpha Detector* (HEPAD) onboard GOES-13 and -15 (e.g. Onsager et al., 1996). In case of event-integrated intensities, we also consider the high-energy (from 80 MeV up to a few GeV) data collected by the PAMELA magnetic spectrometer (Bruno et al., 2018).

The GOES particle detectors are known to be affected by a large background that makes them insensitive to relatively small SEP events, such as many of the events listed by Richardson et al. (2014). On the other hand, they do not suffer from issues related to data gaps and signal saturation during large events. To improve the reliability of their spectroscopic observations we take advantage of the *calibrated* energies derived by Sandberg et al. (2014) for the P2–P5 (<80 MeV) proton energy channels, and by Bruno (2017) for the P6–P11 (>80 MeV) channels, based on the comparison with the STEREO and the PAMELA data, respectively.

SEP intensities are corrected for the quiet-time background (including the galactic cosmic-ray component), estimated from the minimum hourly running averages of intensities registered during a two-month interval prior to the event onset. STEREO spectra are fitted with the Ellison and Ramaty (1985) functional form, given by a power law with an exponential cutoff; near-Earth spectra, extending up to  $\approx 1$  GeV, are fitted with a double power law with an exponential cutoff (see Bruno et al., 2019 for details), that accounts for the high-energy spectral rollover reported by the PAMELA mission at several tens or hundreds of MeV (Bruno et al., 2018). The SEP peak and event-integrated intensity spectra above 4 MeV reconstructed at the three spacecraft locations are reported in Figures 1 and 2, respectively. The spectral fits used in this work are limited to 130 MeV, including a modest extrapolation from the STEREO observations (nominally limited to 100 MeV), to minimize the significant uncertainties affecting the extension to higher energies, especially for hard spectra. In the case of the event #32, large gaps present in STEREO-A data preclude a reliable spectrum reconstruction; to a first approximation, based on the comparison of the respective temporal profiles and the relatively small ( $\approx 32^\circ$ ) longitudinal separation of the two spacecraft, the SEP intensities at STEREO-A are assumed to be equal to those measured by STEREO-B.

Note that measured intensities may include contributions of particles that are locally accelerated at interplanetary shocks – the so-called energetic storm particle (ESP) events. In particular, the resulting peak spectra for a given SEP

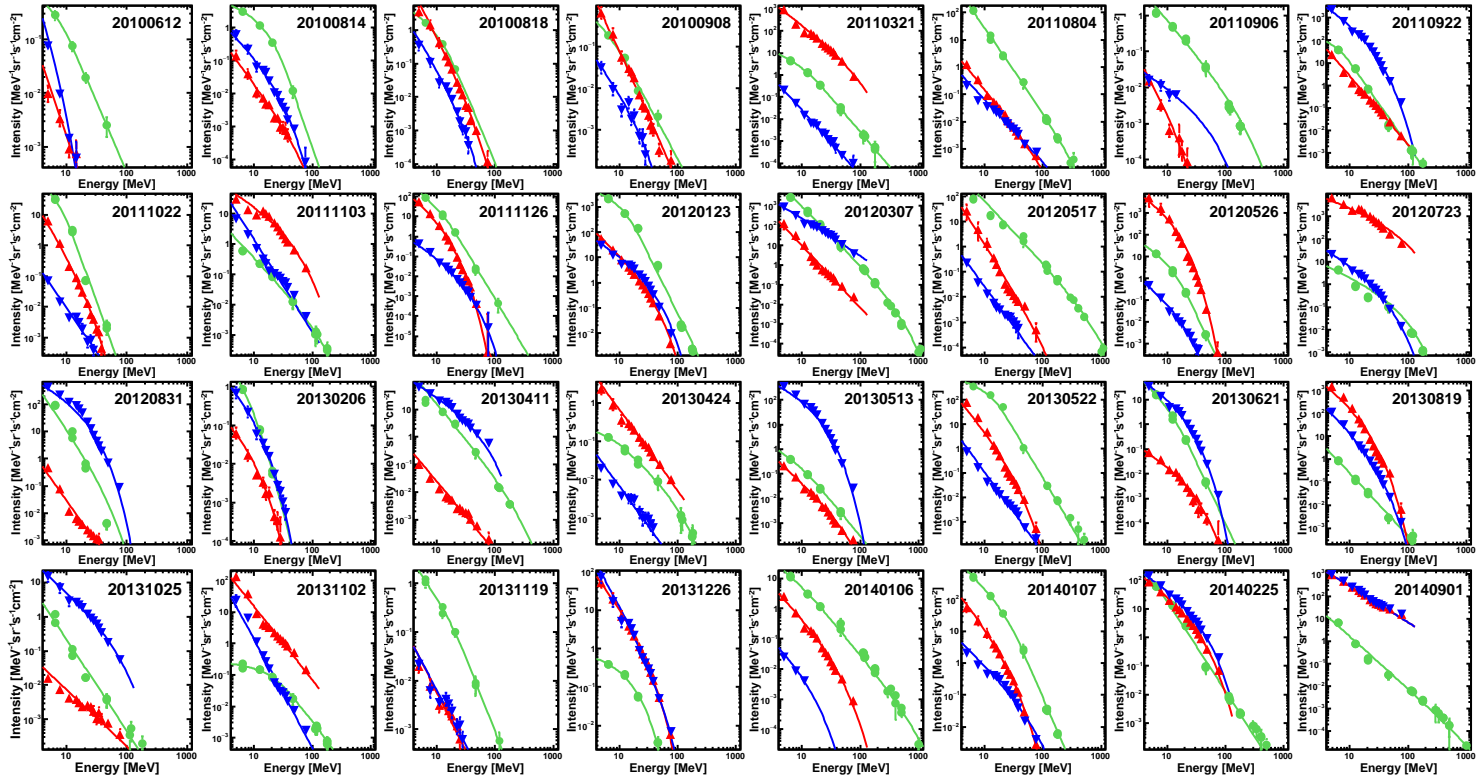


**Figure 1.** Peak intensity spectral fits above 4 MeV based on measurements by GOES-13/15 (green circles), STEREO-A (upward-pointing red triangles) and STEREO-B (downward-pointing blue triangles) during the 32 SEP events reported in Table 1. Each panel reports the date of the corresponding SEP event.

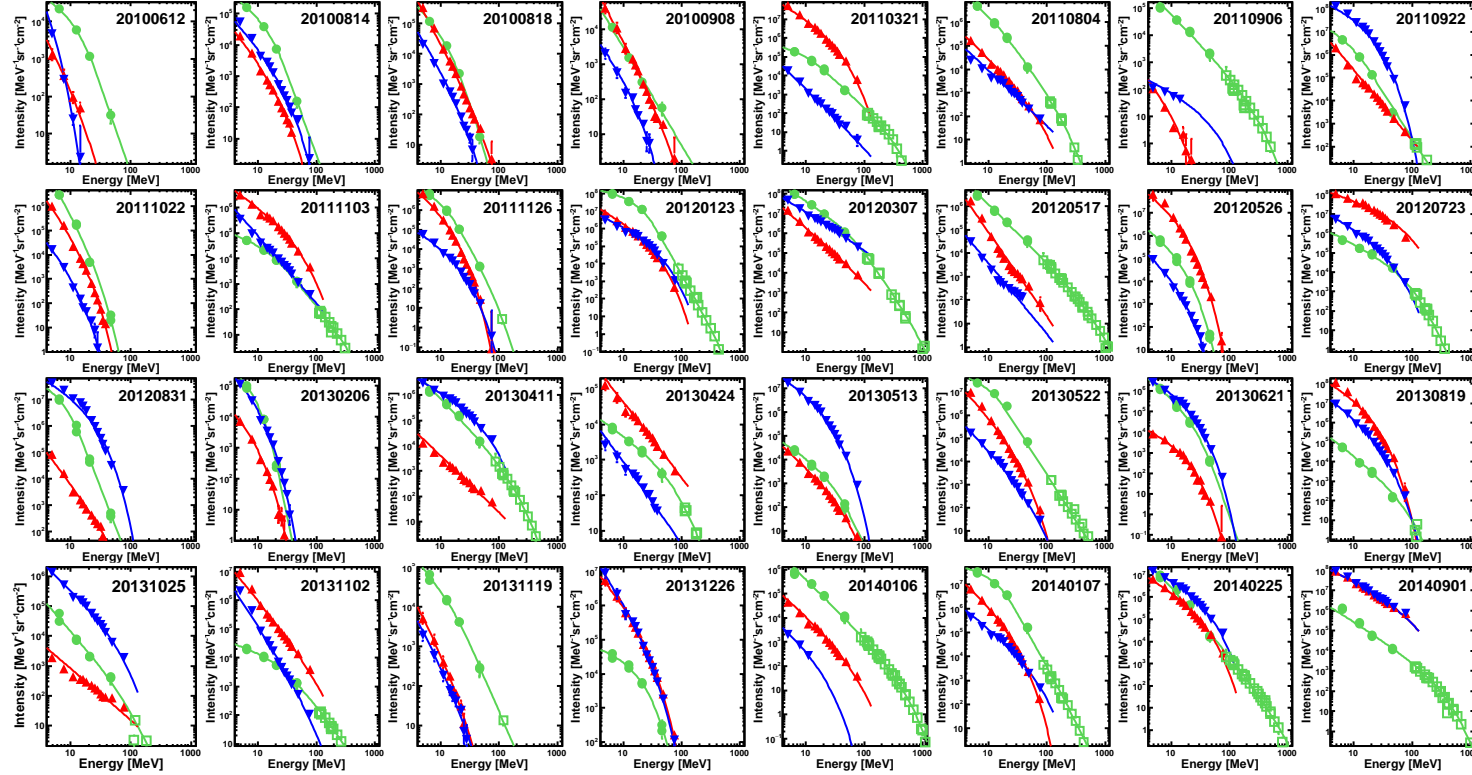


**Figure 2.:** Event-integrated intensity spectral fits above 4MeV based on measurements by GOES-13/15 (green circles), and PAMELA (>80MeV, green squares), STEREO-A (upward-pointing red triangles) and STEREO-B (downward-pointing blue triangles) during the 32 SEP events reported in Table 1. Each panel reports the date of the corresponding SEP event.



event may include a mix of ESP-associated and “first peak” maxima, depending on energy and location. Also, particles from a previous event may be present at a particular spacecraft, or the onset of a new event may constrain the integration interval. These effects may influence the event-integrated intensities, especially for lower energies for which the event durations are longer, but the peak intensities should not be significantly affected since, for the event to be detected, it must significantly exceed the intensity of an ongoing event. Another possible source of uncertainty is related to Forbush-decrease effects, which reduce the particle intensity over a large energy range (e.g. Sanderson et al., 1990).

### 3. SEP Intensity Spatial Distribution

We assume that the peak or event-integrated intensity as a function of proton energy and location can be expressed as

$$\Phi(E, \delta) = \Phi_o(E) G(E, \delta) \quad (2)$$

where  $\Phi_o$  is the maximum intensity and  $G$  is the normalized 2D spatial distribution at 1 AU in terms of the great-circle or spherical distance from the location of the SEP distribution peak ( $\alpha_{\text{sep}}, \beta_{\text{sep}}$ ):

$$\delta = \arccos [\sin(\alpha) \sin(\alpha_{\text{sep}}) + \cos(\alpha) \cos(\alpha_{\text{sep}}) \cos(\beta - \beta_{\text{sep}})], \quad (3)$$

with  $\alpha$  and  $\beta$  being the HGS latitude and longitude. The SEP intensities measured at the three locations – which, for simplicity, are assumed to be isotropic – are, following Cohen, Mason, and Mewaldt (2017) and de Nolfo et al. (2019), fitted by a periodic Gaussian function with form:

$$G(E, \delta) = \frac{1}{3} \left\{ \exp \left[ -\frac{\delta^2(E)}{2\sigma_{\text{sep}}^2(E)} \right] + \exp \left[ -\frac{\delta_+^2(E)}{2\sigma_{\text{sep}}^2(E)} \right] + \exp \left[ -\frac{\delta_-^2(E)}{2\sigma_{\text{sep}}^2(E)} \right] \right\}, \quad (4)$$

where  $\sigma_{\text{sep}}$  is the distribution standard deviation assuming a spherical symmetry ( $\sigma_{\text{sep}}^\alpha = \sigma_{\text{sep}}^\beta = \sigma_{\text{sep}}$ ); the terms associated with

$$\delta_\pm(E) = \arccos [\sin(\alpha) \sin(\alpha_{\text{sep}}(E)) + \cos(\alpha) \cos(\alpha_{\text{sep}}(E)) \cos(\beta - \beta_{\text{sep}}(E) \pm 2\pi)] \quad (5)$$

ensure that  $G(\delta) = G(\delta \pm 2\pi)$ , accounting for the contribution from particles propagating at angles  $>180^\circ$  from the center of the distribution, which is expected to be non-negligible for widespread events – the use of a non-periodic Gaussian function would lead to an overestimate of the distribution width. The parameters  $\alpha_{\text{sep}}, \beta_{\text{sep}}$ , and  $\sigma_{\text{sep}}$  are functions of particle energy. To a first approximation,  $\alpha_{\text{sep}}$  is assumed to coincide with the latitude of the parent CME direction ( $\alpha_{\text{sep}} = \alpha_{\text{cme}}$ ) or with the flare latitude ( $\alpha_{\text{sep}} = \alpha_{\text{flare}}$ ), if the CME information is not available.

Particle transport along the IMF is accounted for by computing the HGS location ( $\alpha = \alpha_{\text{sc}}, \beta = \beta_{\text{sc}}$ ) of the footpoints of the Parker spiral field lines linking

each spacecraft (hereafter referred as “spacecraft footpoints”), which are mapped ballistically back to  $2.5 R_{\odot}$  (see Appendix A). This value roughly corresponds to the nominal source-surface height beyond which the spiral-model approximation is reasonable (see Lee et al., 2011 and references therein) and, moreover, to the radial distance where highest-energy particles are released from the CME-driven shock (Reames, 2009; Gopalswamy et al., 2013). Thus it is unnecessary to consider using a coronal field model to map these field lines down to their photospheric footpoints. The footpoint calculation is performed at the CME first appearance time, by using the average solar-wind speed measured in the previous 30-minute interval.

In general, as a result of the Sun’s rotation axis’ tilt of about  $7.25^{\circ}$  from perpendicular to the Ecliptic plane, the spacecraft-footpoint locations do not lie in the solar equatorial plane ( $\alpha_{sc} \neq 0$ ). Accordingly, projection effects are accounted for by multiplying measured SEP intensities by

$$K_{\alpha}(E) = \exp \left[ \frac{\delta_{sc}^2(E) - \delta_{sc,0}^2(E)}{2\sigma_{sep}^2(E)} \right], \quad (6)$$

where  $\delta_{sc}$  and  $\delta_{sc,0}$  are the great-circle distances of the peak of the SEP spatial distribution from the spacecraft-footpoint location ( $\alpha=\alpha_{sc}$ ,  $\beta=\beta_{sc}$ ) and from their projection in the solar equatorial plane ( $\alpha=0$ ,  $\beta=\beta_{sc}$ ), respectively. We note that, even though the footpoint latitude is typically small, the differences in terms of great-circle distances can be much larger and the associated correction cannot be neglected.

Finally, the spatial distribution parameters  $\Phi_o(E)$ ,  $\beta_{sep}(E)$  and  $\sigma_{sep}(E)$  are derived from the corrected spacecraft measurements by using the projection of Equation 4 in the solar equatorial plane:

$$\Phi_{eq}(E; \beta) = \Phi_o(E) G_{eq}(E; \beta), \quad (7)$$

where

$$G_{eq}(E; \beta) = \frac{1}{3} \exp \left\{ - \frac{\arccos^2 [\cos(\alpha_{cme}) \cos(\beta - \beta_{sep}(E))]}{2\sigma_{sep}^2(E)} \right\} + \dots, \quad (8)$$

with the two terms centered at  $\beta_{sep} \pm 2\pi$  omitted here for brevity. Since  $\sigma_{sep}$  is unknown a priori, the correction factor given by Equation 6 is obtained through an iterative procedure, using  $\sigma_{sep}=43^{\circ}$  as initial value (Richardson et al., 2014), until the fit results become stable.

### 3.1. Results

Results relative to peak and event-integrated intensity distributions as a function of the longitudinal connection angle  $[\beta_{sep}(E) - \beta_{cme}]$  for the 32 analyzed SEP events are shown in Figures 3 and 4, respectively. Negative/positive angles correspond to locations eastward/westward of the CME direction. Depending on the associated uncertainties, SEP spectral fits shown in Figures 1 and 2 are interpolated at up to 12 logarithmically spaced energy values between 10 and

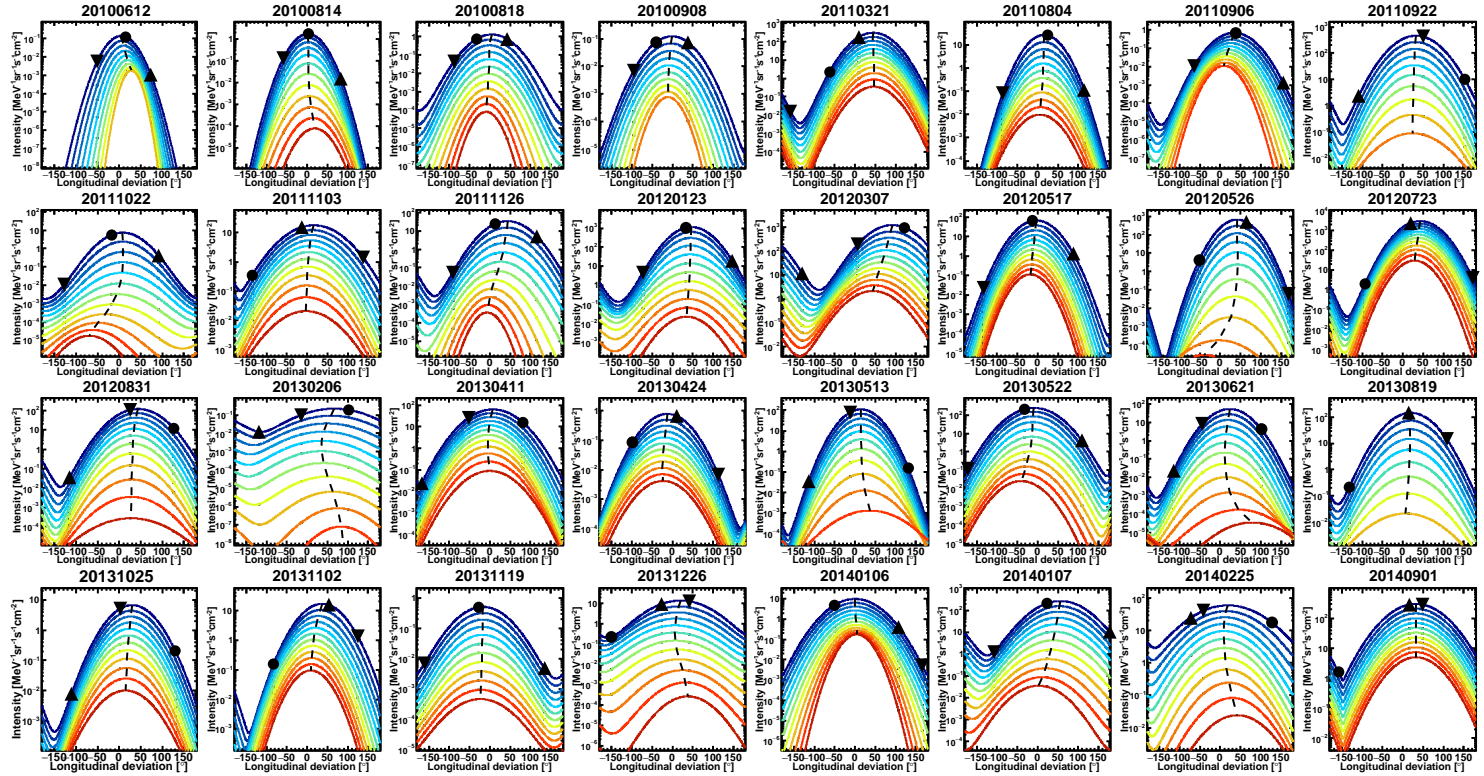


**Figure 3.** 1 AU spatial distribution of the 32 SEP events used in the analysis (Equation 7) determined from the fits of the peak intensities measured by GOES (circles) and STEREO-A/B (triangles), as a function of the longitudinal deviation between the spacecraft magnetic footpoints (estimated at CME onset and at  $2.5 R_{\odot}$  height) and the CME direction. Each panel corresponds to a different SEP event in Table 1. The color code refers to 12 logarithmically spaced energy values between 10 and 130 MeV. The distributions are centered at the peak connection angle evaluated at 10 MeV; the dashed lines are the curves linking the distribution peaks at different energies.

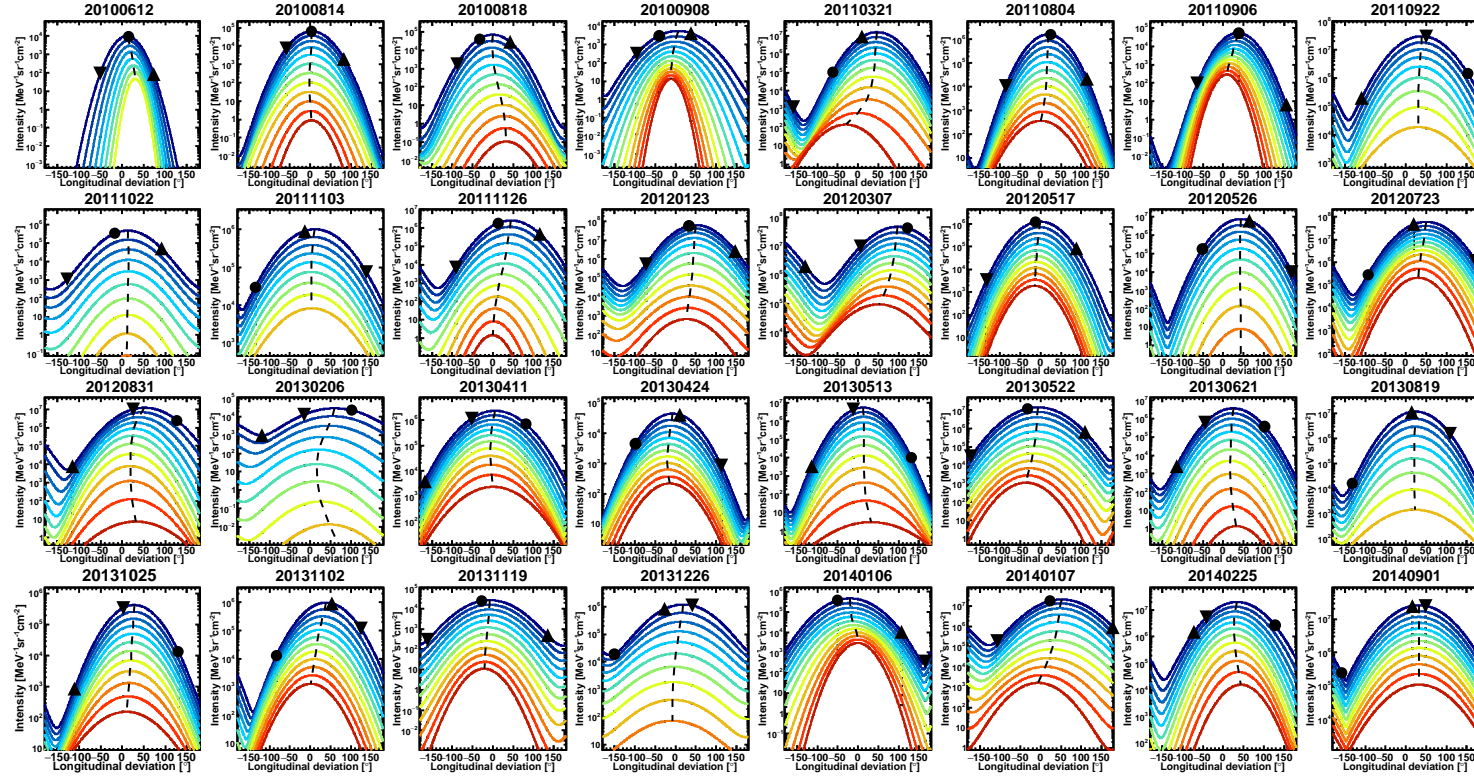


**Figure 4.** 1 AU spatial distribution of the 32 SEP events used in the analysis (Equation 7) determined from the fits of the event-integrated intensities measured by GOES/PAMELA (circles) and STEREO-A/B (triangles), as a function of the longitudinal deviation between the spacecraft magnetic footpoints (estimated at CME onset and at  $2.5 R_{\odot}$  height) and the CME direction. Each panel corresponds to a different SEP event in Table 1. The color code refers to 12 logarithmically spaced energy values between 10 and 130 MeV. The distributions are centered at the peak connection angle evaluated at 10 MeV; the dashed lines are the curves linking the distribution peaks at different energies.

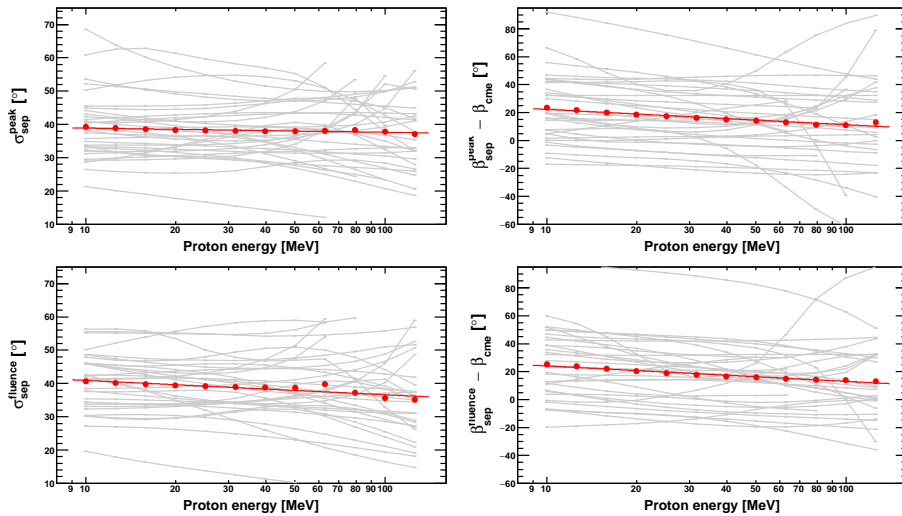


**Figure 5.** Energy dependence of the spatial distribution standard deviation [ $\sigma_{\text{sep}}$ ; left panels] and of the longitudinal deviation [ $\beta_{\text{sep}} - \beta_{\text{cme}}$ ; right panels] from the Gaussian fits of peak and event-integrated intensities (top and bottom panels, respectively). Each gray line corresponds to a different SEP event. The red points are the values averaged over the whole SEP event sample, with the red lines the corresponding fits based on Equations 9–10.

130 MeV (indicated by the line color) and used to reconstruct the corresponding spatial distributions. The three markers denote the longitudinal deviation of the spacecraft footpoints (circles=GOES/PAMELA, triangles=STEREO-A/B). The dashed lines are the curves linking the distribution peaks at different energies. Both of the locations of the peaks and the widths of the distributions show some energy dependences that vary from event to event and deserve further investigation in a separate study.

Figure 5 shows the energy distributions of the related  $\beta_{\text{sep}}$  and  $\sigma_{\text{sep}}$  parameters, for both peak (top panels) and event-integrated (bottom panels) intensities. Significant event-to-event variations can be noted. Investigating their causes is beyond the scope of this study but they might, for example, include contributions from overlapping events or local shock-associated particles at certain spacecraft and energies. In addition, the connection angle of a given spacecraft might be influenced by the presence of interplanetary magnetic structures between the source and the spacecraft location. While such effects introduce significant uncertainties in the estimates of the spatial extent of some SEP events, they are an integral part of the average SEP event properties observed at 1 AU and, as such, are included when constructing the empirical model.

For each proton energy, mean values  $\bar{\beta}_{\text{sep}}$  and  $\bar{\sigma}_{\text{sep}}$  are obtained by averaging over the selected SEP event sample (red points). In order to parameterize their energy dependence, the mean-value distributions are fitted with the functions

$$\bar{\beta}_{\text{sep}}(E) - \beta_{\text{cme}} = \beta_0 - \beta_1 \log(E), \quad (9)$$

**Table 2.** Best-fit parameters for Equations 9–10 derived for both peak and event-integrated intensities.

	$\beta_0$	$\beta_1$	$\sigma_0$	$\sigma_1$
Peak intensities	$3.38 \times 10^1$	$5.11 \times 10^0$	$4.05 \times 10^1$	$5.20 \times 10^{-1}$
Event-int. intensities	$3.52 \times 10^1$	$4.81 \times 10^0$	$4.52 \times 10^1$	$1.87 \times 10^0$

where  $\beta_{\text{cme}}$  is the longitude associated with the CME direction – or the flare longitude if the CME information is not available – and

$$\bar{\sigma}_{\text{sep}}(E) = \sigma_0 - \sigma_1 \log(E). \quad (10)$$

The derived best-fits are denoted by the red curves in Figure 5, with the corresponding parameters  $(\beta_0, \beta_1)$  and  $(\sigma_0, \sigma_1)$  reported in Table 2.

Consistent with previous studies (e.g. Cohen, Mason, and Mewaldt, 2017), the standard deviation  $\bar{\sigma}_{\text{sep}}$  is found to decrease with increasing proton energy, although the variation is relatively small for peak intensities. In addition, the peak of the spatial distribution is, on average, located on field lines with footpoints located westward of the CME direction, and tends to move eastward with increasing energy, so that highest-energy protons are found on field lines with footpoints close to the CME direction.

#### 4. Dependence of SEP Intensity on CME Speed

Similar to Richardson et al. (2014) and Richardson, Mays, and Thompson (2018), we assume that SEP intensity is correlated with the parent CME speed. We do not consider the CME angular widths as they tend to be correlated with the speeds (e.g. Figure 8 of Richardson, von Rosenvinge, and Cane, 2015). Since the SEP intensity–CME speed correlation is energy-dependent (as shown below), we can include this dependence in the parameterization of the SEP spatial distribution maximum intensity  $\Phi_o(E) = \Phi_o(E, V_{\text{cme}})$ , according to the formula

$$\Phi_o(E, V_{\text{cme}}) = \Psi_{\text{cme}}(E) \exp(\Lambda_{\text{sep}}(E) V_{\text{cme}}), \quad (11)$$

where

$$\Psi_{\text{cme}}(E) = \psi_0 (E/E_0)^{-\psi_1} \exp(-E/E_r) \quad (12)$$

and

$$\Lambda_{\text{cme}}(E) = \lambda_0 (E/E_0)^{\lambda_1} \quad (13)$$

account for the energy dependence, with  $E_0=10$  MeV the threshold energy and  $E_r=300$  MeV the cutoff energy. The spectral form in Equation 12 is that proposed by Ellison and Ramaty (1985); the  $E_r$  value is assumed ad hoc to reproduce the SEP spectral rollover reported at high energies by the PAMELA experiment (see Bruno et al., 2018 for details), providing a reasonable description of intensities beyond 130 MeV.

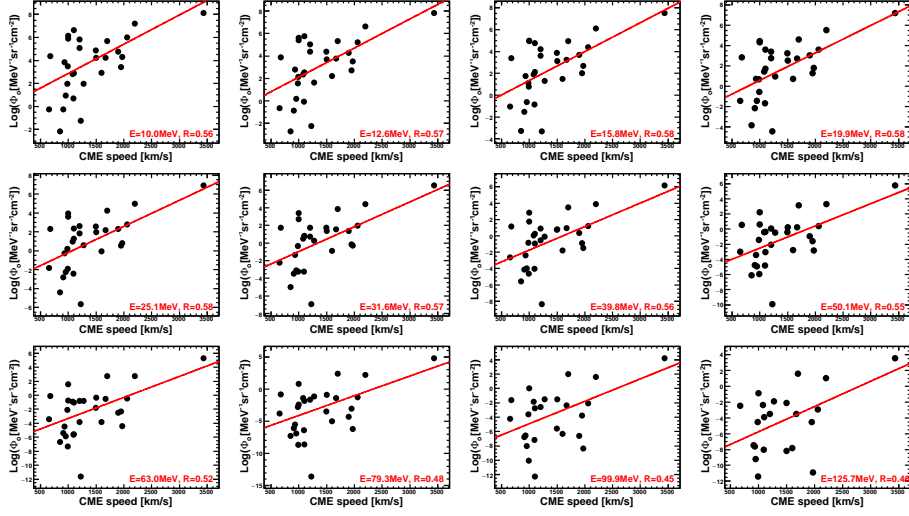


**Figure 6.** Distribution of SEP peak-intensity maxima [ $\log(\Phi_0)$ ] as a function of CME speed [ $V_{\text{cme}}$ ], for 12 energy values between 10 and 130 MeV. The corresponding regression lines are also reported, along with the correlation factor  $R$  values.

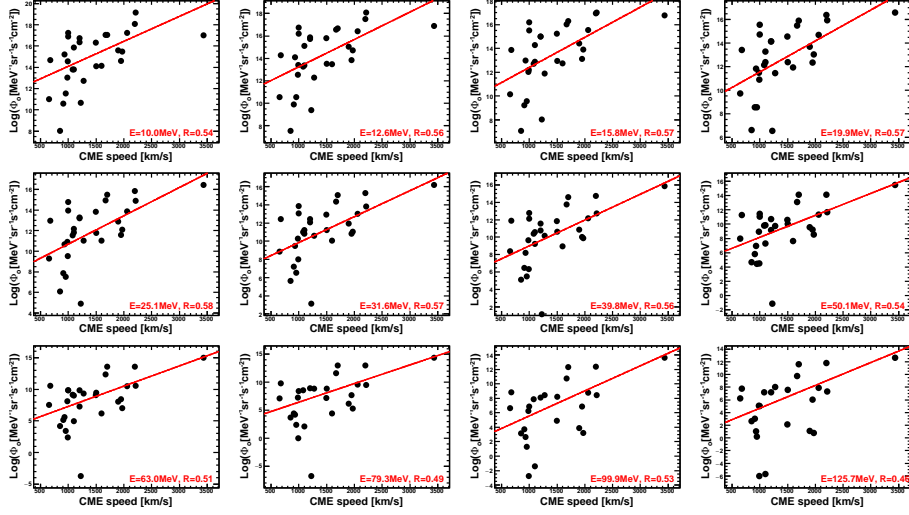


**Figure 7.** Distribution of SEP event-integrated-intensity maxima [ $\log(\Phi_0)$ ] as a function of CME speed [ $V_{\text{cme}}$ ], for 12 energy values between 10 and 130 MeV. The corresponding regression lines are also reported, along with the correlation factor  $R$  values.

The free parameters  $(\psi_0, \psi_1)$  and  $(\lambda_0, \lambda_1)$  are estimated as follows. The calculation involves 29 out of the 32 selected SEP events reported in Table 1 for which the CME information is available. First, for each energy value  $i=1,12$ , a linear fit of the  $\log(\Phi_{0,i})$  versus  $V_{\text{cme}}$  distribution is performed, deriving the individual  $\Psi_{\text{cme},i}$  and  $\Lambda_{\text{cme},i}$  parameters (see Figures 6 and 7). As often noted in other studies of SEP intensities versus CME speeds, there is a large spread

**Table 3.** Best-fit parameters for Equations 12 and 13 derived for both peak and event-integrated intensities.

	$\psi_0$	$\psi_1$	$\lambda_0$	$\lambda_1$
Peak intensities	$1.50 \times 10^0$	$3.61 \times 10^0$	$2.55 \times 10^{-3}$	$9.01 \times 10^{-2}$
Event-int. intensities	$1.31 \times 10^5$	$4.06 \times 10^0$	$2.35 \times 10^{-3}$	$1.69 \times 10^{-1}$

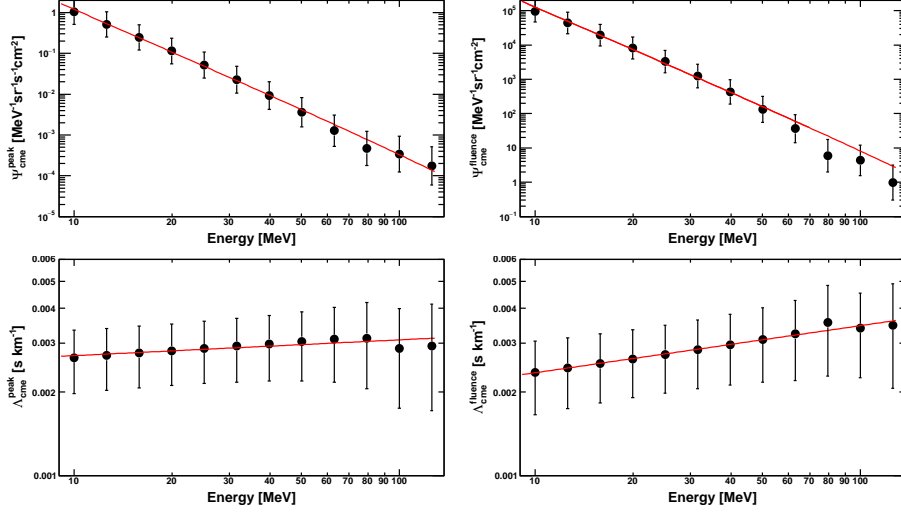


**Figure 8.** Distribution of  $\Psi_{\text{cme}}$  and  $\Lambda_{\text{cme}}$  values (top and bottom panels, respectively) from the individual fits performed at different proton energies, for peak intensities (left panels, from Figure 6) and event-integrated intensities (right panels, from Figure 7). The red curves represent the fits with Equations 12-13.

about the best-fit line at each energy for this sample of events, but the general trends are evident. At some energies, the fit appears to be dominated by event #16 associated with an unusually fast CME, but it is also consistent with the trend evident in the remaining events. Then, the distributions of the  $\Psi_{\text{cme},i}$  and  $\Lambda_{\text{cme},i}$  values as a function of proton energy are fitted by using the functional forms in Equations 12 and 13 respectively, as shown in Figure 8, providing an estimate of the best-fit parameters  $(\psi_0, \psi_1)$  and  $(\lambda_0, \lambda_1)$ , reported in Table 3.

## 5. Model Uncertainties

The uncertainty in the predicted SEP event-integrated or peak intensity  $\Phi(E, V_{\text{cme}})$  can be obtained by propagating the errors on the spacecraft footpoint location, the CME speed, and the energy-dependent  $\bar{\sigma}_{\text{sep}}$ ,  $\bar{\beta}_{\text{sep}}$ ,  $\Psi_{\text{cme}}$  and  $\Lambda_{\text{cme}}$  values given by Equations 9–10 and 12–13, according to the standard formula:

$$\delta\Phi = \left\{ \left[ \frac{\partial\Phi}{\partial\bar{\sigma}_{\text{sep}}} \delta\bar{\sigma}_{\text{sep}} \right]^2 + \left[ \frac{\partial\Phi}{\partial\alpha_{\text{cme}}} \delta\alpha_{\text{cme}} \right]^2 + \left[ \frac{\partial\Phi}{\partial\bar{\beta}_{\text{sep}}} \delta\bar{\beta}_{\text{sep}} \right]^2 + \right. \quad (14)$$



$$\left[ \frac{\partial \Phi}{\partial \alpha_{sc}} \delta \alpha_{sc} \right]^2 + \left[ \frac{\partial \Phi}{\partial \beta_{sc}} \delta \beta_{sc} \right]^2 + \left[ \frac{\partial \Phi}{\partial \Psi_{cme}} \delta \Psi_{cme} \right]^2 + \left[ \frac{\partial \Phi}{\partial \Lambda_{cme}} \delta \Lambda_{cme} \right]^2 + \left[ \frac{\partial \Phi}{\partial V_{cme}} \delta V_{cme} \right]^2 \Bigg\}^{1/2}.$$

All parameters associated with the aforementioned quantities (e.g.  $\sigma_0$  and  $\sigma_1$  in the case of  $\bar{\sigma}_{sep}$ ) are assumed to be dependent, and related errors are estimated by using the corresponding covariance matrices. Conservatively, for CME parameter estimates based on three-spacecraft observations, a  $5^\circ$  and  $10^\circ$  error is assumed on  $\alpha_{cme}$  and  $\beta_{cme}$ , respectively, while a 20% uncertainty is associated with  $V_{cme}$ ; for two-spacecraft measurements (i.e. after the termination of STEREO-B), the uncertainties are  $10^\circ$ ,  $15^\circ$ , and 30%, respectively (L. Mays, private communication, 2020). Finally, a 200 MeV error is associated with  $E_r$ . As discussed in Appendix A, the uncertainty in the footpoint longitude accounts for a  $100 \text{ km s}^{-1}$  error associated with the solar-wind speed estimate and includes a  $25^\circ$  error accounting for interplanetary transport effects ignored by the model, such as the influence of magnetic fluctuations (e.g. Ippolito et al., 2005) and solar wind structures (e.g. Lario and Karelitz, 2014; Masson et al., 2012), or the propagation across the nominal Parker spiral magnetic field (e.g. Jokipii, 1966; Dalla et al., 2013; Laitinen et al., 2016). Similarly, a  $10^\circ$  error is assumed on the footpoint latitude accounting for the deviations from the spiral model approximation out of the equatorial plane and effects related to the differential changes across the solar surface. The total error  $\delta \Phi$  increases with  $V_{cme}$ , and it is dominated by the uncertainties in  $\Psi_{cme}$  and  $\Lambda_{cme}$ , as a consequence of the spread in the  $\Phi_o$  versus  $V_{cme}$  distributions in Figures 6 and 7.

## 6. Model Testing and Caveats

In order to test the empirical SEP prediction model based on the parameterization of the sample of SEP events discussed in previous sections, we compare the observed and calculated spectra for 20 events not used to derive the model parameters. The selected sample, listed in Table 4, essentially comprises energetic events detected between 2011 and 2017 at Earth and, possibly, at one STEREO spacecraft – with the exception of the 30 September 2013 three-spacecraft event – as a consequence of a relatively narrow spatial distribution compared to the spacecraft separation, a large background component from a previous event that precludes a direct measurement of the event, significant data gaps (e.g. between September 2014 and November 2015), or after the loss of contact with STEREO-B in October 2014. This last subset includes the 10 September 2017 event, associated with the 72nd GLE (Bruno et al., 2019).

The SEP peak and event-integrated spectra for these 20 events reconstructed at Earth and STEREO are displayed in Figures 9–10 and 11–12, respectively. Near-Earth measurements, extending up to  $\approx 1 \text{ GeV}$ , are based on the GOES-13/15 EPEAD/HEPAD sensors and, in case of event-integrated intensities, on the high-energy PAMELA data. STEREO observations, limited to 100 MeV, rely on the SIT, LET, and HET detectors. The corresponding model predictions

**Table 4.** List of CMEs associated with the SEP events used for testing the empirical model. The first column is the event number. Columns 2–5 report the CME first appearance time [UT], space speed [km s<sup>-1</sup>], angular width [°] and direction from the DONKI catalog. The next three columns list the location of the footpoints of the Parker spiral field lines crossed by each spacecraft (STEREO-A/B and GOES/PAMELA) at CME onset, mapped ballistically back to 2.5 R<sub>⊙</sub>. Footpoints locations and CME directions are expressed in terms of HGS latitudes/longitudes. The dots (...) indicate no STEREO data available.

#	Onset time	CME			Spacecraft footpoints		
		Speed	Width	Direction	STB	Earth	STA
1	2011-03-07T20:12	1980	90	N17W50	N01E16 <sup>b</sup>	S07W55	S00W153
2*	2011-06-07T06:50	1400	92	S25W52	S07E48 <sup>b</sup>	N00W55	N07W122 <sup>b</sup>
3	2011-08-09T08:30	1175	40	S12W62	S03E10 <sup>a</sup>	N06W42	N02W138
4*	2012-01-27T16:39	2200	110	N40W75	N06E56 <sup>b</sup>	S05W47	S02W160
5*	2012-03-13T17:52	2250	120	N25W43	N02E63 <sup>b</sup>	S07W37	N03W162 <sup>b</sup>
6*	2012-07-06T23:12	1200	80	S35W65	S07E66 <sup>a</sup>	N03W53	N03W170
7*	2012-07-08T16:48	1000	60	S17W74	S07E58 <sup>a</sup>	N03W56	N03W177
8*	2012-07-12T16:54	1300	130	S13W06	S07E46	N04W50	N03W160 <sup>b</sup>
9	2012-07-17T14:24	1100	90	S30W54	S06E73 <sup>a</sup>	N04W55	N02E174
10*	2012-07-19T05:36	1550	120	S14W94	S06E58 <sup>a</sup>	N04W53	N02E176 <sup>b</sup>
11*	2013-09-29T22:40	1100	140	N26W38	S02E46	N06W87	S07E129
12*	2013-10-28T14:12	1100	70	N27W80	N00E69	N04W84 <sup>b</sup>	S06E158 <sup>b</sup>
13	2013-11-07T10:39	2100	184	S13E135	N00E101	N04W67 <sup>b</sup>	S06E171
14	2013-12-28T18:00	769	130	S01W101	N05E73 <sup>b</sup>	S02W79	S00E151 <sup>b</sup>
15	2014-02-20T08:00	854	80	S04W79	N07E81 <sup>a</sup>	S07W45	N05E164 <sup>b</sup>
16*	2014-04-18T13:09	1400	90	S34W10	N04E76 <sup>a</sup>	S05W60	N06E142 <sup>a</sup>
17*	2014-09-10T18:18	1400	90	N15W10	S06E95	N07W66	S07E129 <sup>b</sup>
18	2015-06-21T02:48	1250	114	N07E08	...	N01W74	...
19	2017-07-14T01:36	750	98	S09W40	...	N04W58	S07E86 <sup>a</sup>
20	2017-09-10T16:09	2650	108	S12W85	...	N07W46	S04E69

\*Associated with SEP events observed by PAMELA (Bruno et al., 2018). <sup>a</sup>No significant SEP signal. <sup>b</sup>High background from an ongoing SEP event.

between 10–130 MeV are marked by the solid red lines, while the extrapolation of each spectrum outside the nominal energy range is denoted by the dotted blue lines. The gray bands indicate the one- $\sigma$  uncertainty associated with the predicted spectra, as discussed above. For comparison, the green stars in Figures 9–10 mark the 14–24 MeV peak intensities estimated with the model by Richardson, Mays, and Thompson (2018), which are generally consistent with the reported results.

While the model is obviously unable to account for the complex event-to-event variations involving, for instance, effects related to pre-existing conditions both in the corona and the interplanetary medium, the calculated spectra are in a reasonable agreement with the observational data within model uncertainties, in terms of both spectral shapes and absolute intensities. The largest differences are reported for the 10 September 2017 SEP event at STEREO-A, for which measured intensities are underestimated by more than two orders of magnitude. Bruno et al. (2019) showed that the peak intensities registered by STEREO-A at most energies were associated with the passage of a co-rotating

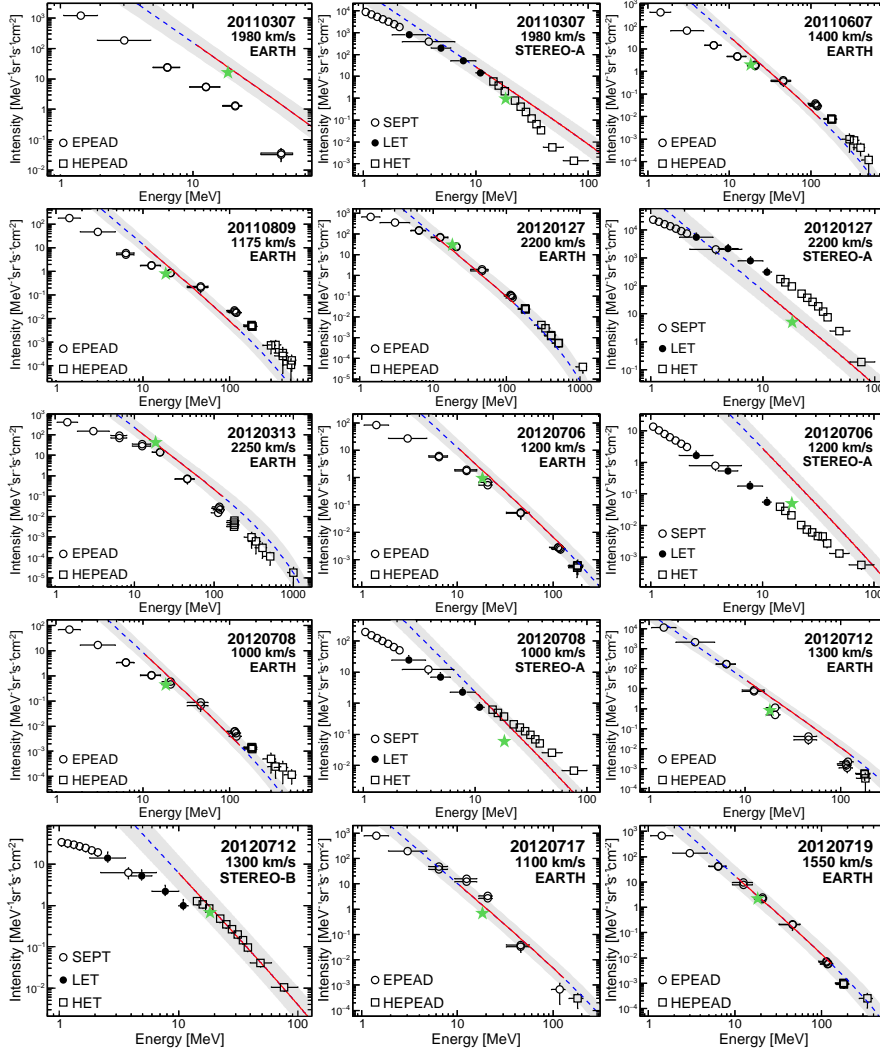


**Figure 9.** Peak spectra of the test SEP events #1–10 listed in Table 4, measured at Earth and/or STEREO. The event date, the related CME speed and the spacecraft location are reported in each panel. The red lines are the predicted spectra between 10–130 MeV; the dashed blue lines are the extrapolations to lower/higher energies. The gray band denotes the one- $\sigma$  uncertainty associated with the model prediction. For a comparison, the green stars are the 14–24 MeV peak intensities based on the model by Richardson, Mays, and Thompson (2018).

interaction region. In addition, given the  $\approx 154^\circ$  longitudinal deviation between the spacecraft footpoint location and the CME direction, it can be speculated that this discrepancy may be ascribed to an exceptionally extended SEP source – compared to the  $\lesssim 40^\circ$   $\bar{\sigma}_{\text{sep}}$  value assumed by the model – in combination with significant transport effects such as cross-field diffusion and IMF co-rotation (see Bruno et al., 2019). In general, the predicted spectra tend to be softer than

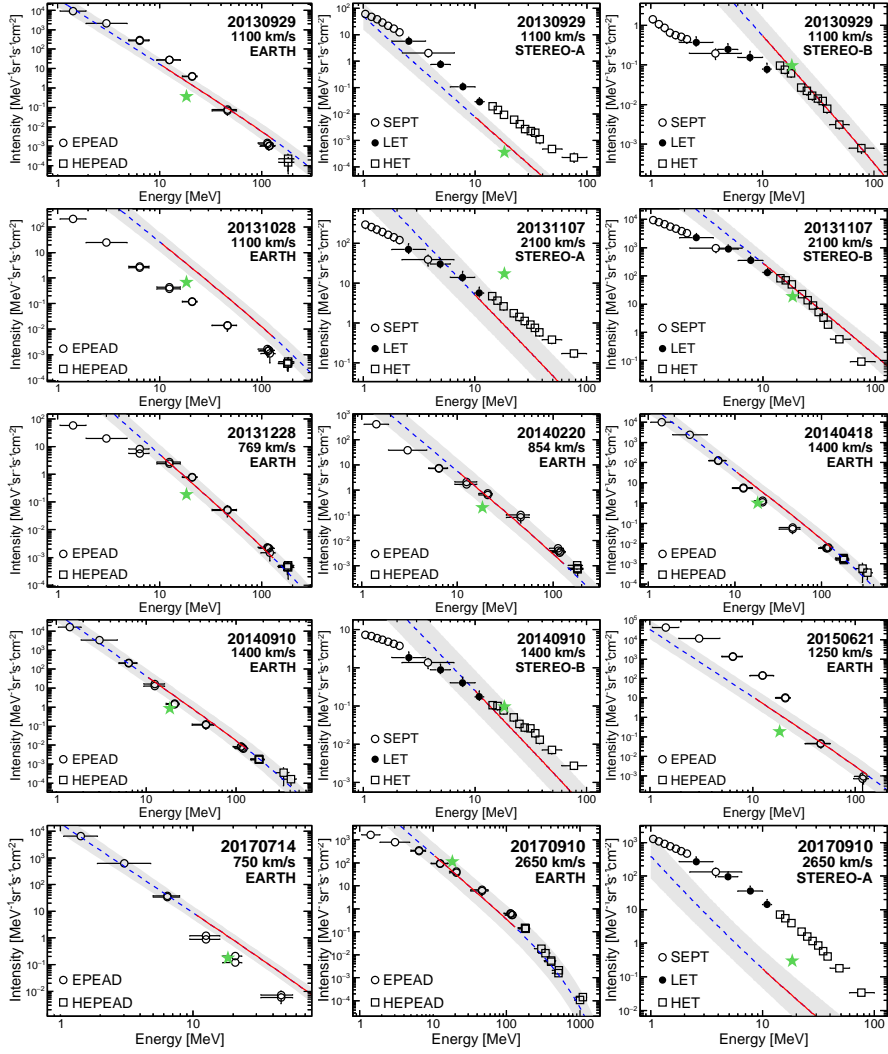


**Figure 10.** Peak spectra of the test SEP events #11–20 listed in Table 4, in the same format as Figure 9.

observed at the lower end of the energy range, but this is due to the relatively simple spectral form assumed, which does not account for the spectral break that is often observed at a few or tens of MeV (see, e.g., Zhao, Zhang, and Rassoul, 2016 and references therein). Another limitation is related to the fact that model parameters have been derived by using widespread (three-spacecraft) SEP events, which are usually the most intense. Although not demonstrated by the events in Figures 9–12, the model, similar to that of Richardson, Mays, and Thompson (2018), is likely to overestimate the intensity of events associated with relatively slow ( $\lesssim 600 \text{ km s}^{-1}$ ) CMEs.

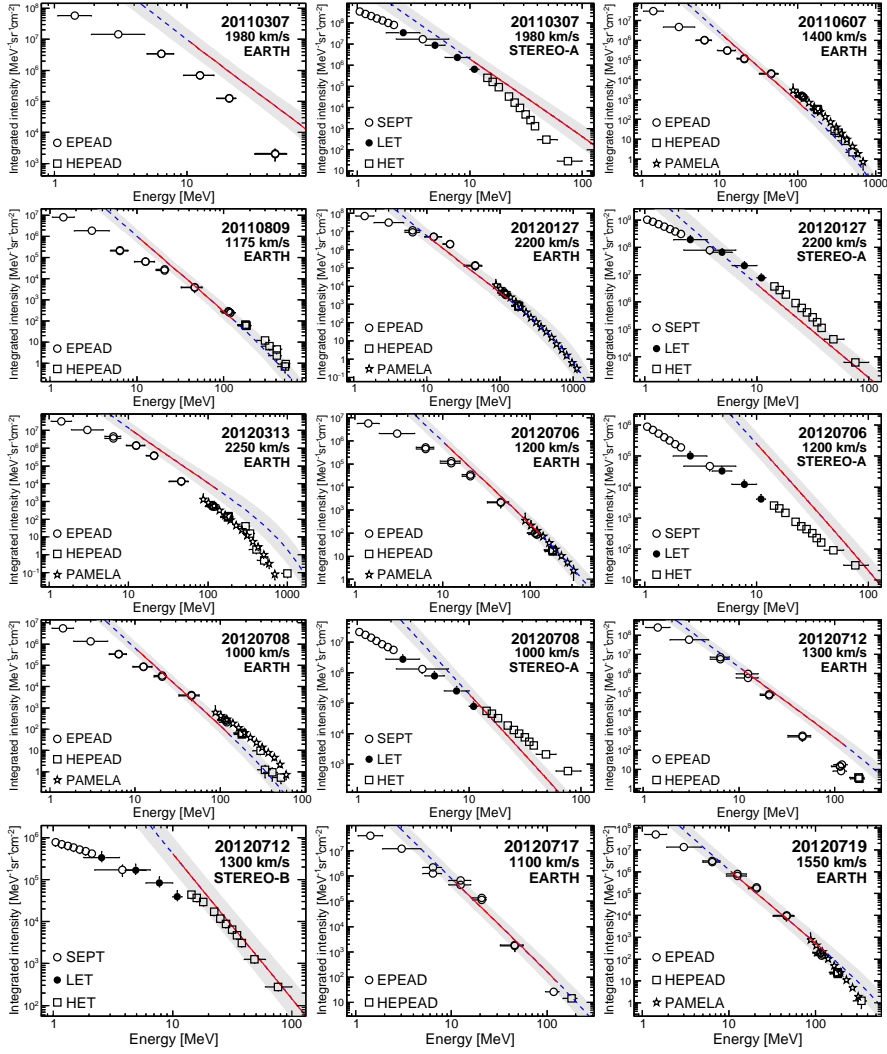


**Figure 11.** Event-integrated spectra of the test SEP events #1–10 listed in Table 4, measured at Earth and/or STEREO (see Figure 9 for details). In this case, the experimental data include the high-energy observations of the PAMELA experiment (when available), marked by empty stars.

## 7. Summary and Conclusions

We presented a new empirical model for predicting SEP event-integrated and peak spectra that is derived from a parameterization of SEP events at 1 AU based on multi-point spacecraft observations from the twin STEREOs and near-Earth assets, including GOES-13/15 instruments and the PAMELA experiment. In particular, the data sample used includes 32 SEP events occurring between 2010 and 2014, with a statistically significant proton signal at energies in excess

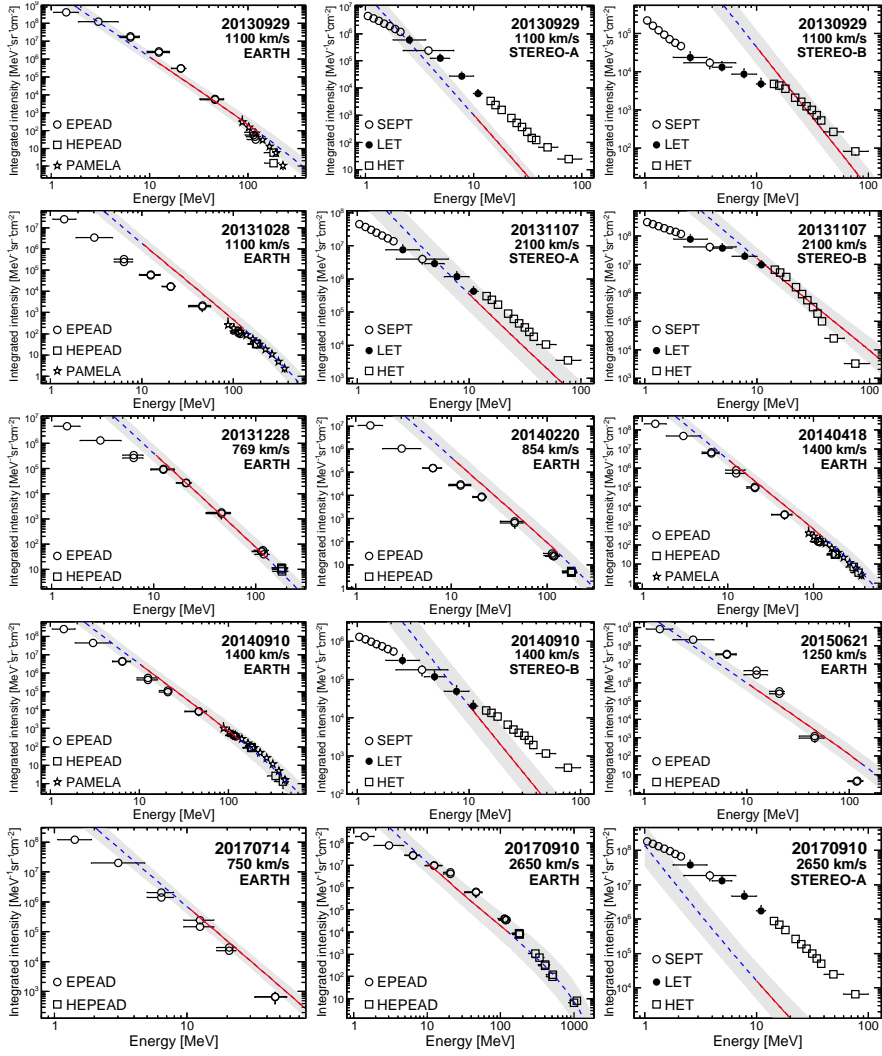


**Figure 12.** Event-integrated spectra of the test SEP events #11–20 listed in Table 4, in the same format as Figure 11.

of a few tens of MeV, unambiguously recorded at three spacecraft locations. The SEP-event spatial distributions in a relatively wide energy range (10–130 MeV) have been reconstructed by using a 2D Gaussian functional form accounting for particle-intensity dependence on both heliospheric longitude and latitude.

This study has also summarized the spatial distributions of these SEP events as a function of energy, and further investigation is required to understand the conditions that give rise to the event-to-event variations. On average, the standard deviation  $\sigma_{\text{sep}}$  decreases with increasing energy, from  $\approx 39^\circ$  at 10 MeV to  $\approx 38^\circ$  at 130 MeV for the peak intensities, and from  $\approx 41^\circ$  to  $\approx 36^\circ$  for the event-integrated intensities, consistent with the widths found in previous studies. As

discussed by Cohen, Mason, and Mewaldt (2017), this trend can be interpreted in terms of several acceleration and/or transport processes. For instance, lower-energy particles are believed to be efficiently accelerated over a more extended shock region and for a longer time as the shock propagates in the interplanetary space, and they experience more field-line co-rotation, especially during long-duration events, resulting in a broader angular range of intersected field lines. However, the near energy-independence of the corresponding  $\sigma_{\text{sep}}$  value suggests that these effects are less important for peak intensities, and that further factors may determine the width. For example, as mentioned in Section 2.2, measured event-integrated intensities are more affected by the contribution from local shock-associated particles and overlapping SEP events, which is expected to be larger at lower energies. In addition, the average distribution peak has been found to be located on field lines with footpoints to the West of the associated CME direction, with the longitudinal deviation increasing with decreasing particle energy. This effect might be accounted for, at least in part, if the high-energy particles were released when the shock is still close to the Sun and hence have peak intensity on field lines with footpoints close to the CME longitude (see Lario, Roelof, and Decker, 2014). The low-energy distribution may be dominated by particles accelerated by the shock as it moves out through the solar wind, with the largest particle intensities close to the nose of the shock. The nose then intercepts field lines that have footpoints lying to the West of the CME longitude. Figures 10 and 11 of Cane, Reames, and von Rosenvinge (1988) also demonstrate a similar trend in proton peak intensities with the longitude of the solar event over a range of energies (1–327 MeV) for a large sample of events: at low energies the intensity peaks tend to be associated with the passage of shocks following solar events in a broad region around central meridian, whereas at high energies peak intensities are generally associated with well-connected western-hemisphere events and unrelated to shock passage.

We also explored the well-known correlation of particle intensities with the parent CME speed, used as a proxy of the shock acceleration efficiency, deriving an energy-dependent parameterization. The results obtained for the analyzed sample of events were used to create a novel empirical model predicting both SEP event-integrated and peak spectra at a given 1 AU location, that is a development of the SEPSTER model described by Richardson, Mays, and Thompson (2018). The input parameters are given by the velocity of the CME associated with the event [ $V_{\text{cme}}$ ] and by the connection angle with respect to its direction, based on the DONKI catalog, accounting for the heliographic coordinates ( $\alpha_{\text{sc}}, \beta_{\text{sc}}$ ) of the IMF line linking the source to the observer. The model calculation is based on the following steps.

- i) The *amplitude*  $\Phi_{\text{o}}(E, V_{\text{cme}})$  can be estimated by using Equations 11-13 and the related parameters reported in Table 3.
- ii) Then, the intensity at longitude  $\beta_{\text{sc}}$  in the solar equatorial plane can be derived by multiplying  $\Phi_{\text{o}}(E, V_{\text{cme}})$  by the relative *weight*  $G_{\text{eq}}(E; \beta_{\text{sc}})$  according to Equation 7, with  $\alpha_{\text{sep}} = \alpha_{\text{cme}}$ ;  $\beta_{\text{sep}} = \bar{\beta}_{\text{sep}}$  and  $\sigma_{\text{sep}} = \bar{\sigma}_{\text{sep}}$  are calculated from Equations 9-10 and the parameters reported in Table 2.

- iii) To get the final intensity  $\Phi(E, V_{\text{cme}}; \beta_{\text{sc}})$  at spacecraft location,  $\Phi_{\text{eq}}(E; \beta_{\text{sc}})$  has to be divided by the  $K_{\alpha}$  factor given by Equation 6, accounting for the spacecraft magnetic footpoint latitude.

Prediction uncertainties have been estimated by accounting for uncertainties in the various parameters involved. The model was developed using widespread SEP events associated with  $>600 \text{ km s}^{-1}$  fast CMEs in the DONKI catalog, and for proton energies between 10 and 130 MeV, and it is likely to provide the most reliable calculations for similar events. The spectra predicted by the model have been tested by comparing them with the observed spectra for 20 SEP events that were not used to develop the model. A remarkable agreement is found within the model uncertainties, both in terms of the spectral shapes and absolute values, despite the many potential factors that are neglected in the model but which may influence the particle intensities and cause large event-to-event variations.

One practical issue with the model is related to its reliance on the availability and accuracy of near real-time spacecraft CME measurements. The CME may only just have entered the field of view of a space-based coronagraph by the time energetic particles reach a well-connected spacecraft. However, other schemes such as the Relativistic Electron Alert System for Exploration (REleASE: Posner, 2007; Posner et al., 2009), based on the early arrival of near-relativistic electrons relative to protons, could be used for predicting the onset of such events; the present model is more suitable for making predictions at less well-connected locations or for long-duration events. Furthermore, at present, space-based coronagraph observations are provided by scientific spacecraft such as SOHO and STEREO and are received with delays of hours or even days after detection; subsequent analysis to obtain CME parameters introduces additional delays. Real-time coronagraph measurements such as will be provided by the NOAA *Space Weather Follow On-Lagrange 1* (SWFO-L1) spacecraft will be required to increase the value of CME-driven SEP prediction schemes, combined with an automated CME identification and tracking system. Another aspect is the accuracy of the CME parameter estimates. As noted by Richardson, von Roseninge, and Cane (2015), current CME catalogs using different analysis methods generally disagree on the speeds and widths of individual CMEs associated with SEP events. Also, the availability of observations from more than one viewpoint can improve estimates of the CME parameters. For the events considered here, the DONKI CME parameters were generally based on observations from SOHO and the two STEREOs. However, with the loss of STEREO-B, and with STEREO-A approaching Earth at the time of writing, the range of viewpoints is more limited, increasing the uncertainty in the CME parameters.

As discussed by Richardson, Mays, and Thompson (2018), a major problem with a CME-driven prediction scheme is that only a small fraction of CMEs produce an SEP event that is detected at 1 AU so that the majority of predictions are false. They discuss several ways of increasing the prediction skill of such models by, for example, considering whether Type II or Type III radio emissions accompany the CME, or by just making predictions for those CMEs that exceed a threshold speed or speed and width. This aspect is not considered here, since all of the CMEs in this study were associated with SEP events, but



similar considerations would apply to the current model. In addition, ground-based coronagraph observations might be used to provide an earlier warning of a potential SEP event (St. Cyr, Posner, and Burkepile, 2017). We also plan to explore the possibility of including in the model parameters related to the related flares, or additional features characterizing the SEP events, such as their onset/peak times or their delay with respect to possibly associated electron events.

**Acknowledgments** The DONKI catalog ([ccmc.gsfc.nasa.gov/donki/](http://ccmc.gsfc.nasa.gov/donki/)) is compiled at the CCMC. The GOES, PAMELA and STEREO data are available at [www.ngdc.noaa.gov/stp/satellite/goes/](http://www.ngdc.noaa.gov/stp/satellite/goes/), [www.ssdsc.asi.it/pamela/](http://www.ssdsc.asi.it/pamela/) and [www.srl.caltech.edu/STEREO/](http://www.srl.caltech.edu/STEREO/), respectively. The authors thank M. L. Mays for the assistance with the DONKI database. They acknowledge support from the NASA/HSR program NNH19ZDA001N-HSR, the Goddard Space Flight Center / Internal Scientist Funding Model (ISFM) grant HISFM18, and from the Johnson Space Center / Space Radiation Analysis Group (SRAG) under the Integrated Solar Energetic Proton Alert/Warning System (ISEP) project. I.G. Richardson also acknowledges support from NASA program NNH17ZDA001N-LWS and from the STEREO mission.

**Disclosure of Potential Conflicts of Interest** The authors declare that they have no conflicts of interest.

## Appendix

### A. Estimate of the Magnetic Footpoint Location

The HGS coordinates  $(\alpha_{sc}, \beta_{sc})$  of the footpoint location of the IMF line passing through a given spacecraft can be estimated by assuming a simple 3D Parker spiral model (Parker, 1958). Specifically, the longitude is calculated as:

$$\beta_{sc} \approx b_{sc} + \frac{\Omega_{\odot}}{V_{sw}} (R_{sc} - R'_0) \cos(\alpha_{sc}), \quad (15)$$

where  $b_{sc}$  is the longitude of the spacecraft location,  $R_{sc}$  is its radial distance,

$$R'_0 = R_0 \left[ 1 + \log \left( \frac{R_{sc}}{R_0} \right) \right], \quad (16)$$

with  $R_0 = 2.5 R_{\odot}$  the radius of the “source” surface;  $V_{sw}$  is the solar-wind speed [ $\text{km s}^{-1}$ ] – assumed to be constant and purely radial – and  $\Omega_{\odot}$  is the differential solar rotation rate at the latitude  $\alpha_{sc}$  of the footpoint location:

$$\Omega_{\odot} = A - B \sin^2(\alpha_{sc}) - C \sin^4(\alpha_{sc}), \quad (17)$$

with  $A = 2.972 \pm 0.010 \mu\text{rad s}^{-1}$ ,  $B = 0.484 \pm 0.038 \mu\text{rad s}^{-1}$  and  $C = 0.361 \pm 0.051 \mu\text{rad s}^{-1}$  (Snodgrass and Ulrich, 1990); in particular, the value of  $A$  is related to the sidereal rotation period at the equator ( $\approx 24.47$  days). The footpoint latitude  $\alpha_{sc}$  is assumed to coincide with the heliographic latitude of the central point of the

solar disk as seen by the spacecraft, accounting for the Sun's rotation axis' tilt of about  $7.25^\circ$  relative to the Ecliptic plane. In general, at large radial distances the Parker spiral IMF is simplified as an Archimedes spiral by neglecting the logarithmic term ( $R_{\text{sc}} - R'_0 \approx R_{\text{sc}} - R_0$ ).

The uncertainty associated with the footpoint longitude can be calculated as:

$$\delta\beta_{\text{sc}} = \sqrt{(\delta\beta_{\text{sw}})^2 + (\delta\beta_{\text{tra}})^2}, \quad (18)$$

where

$$\delta\beta_{\text{sw}} = \frac{(R_{\text{sc}} - R'_0) \cos(\alpha_{\text{sc}})}{V_{\text{sw}}} \sqrt{\left[ \left( \frac{\partial\Omega_{\odot}}{\partial\alpha_{\text{sc}}} - \tan(\alpha_{\text{sc}}) \Omega_{\odot} \right) \delta\alpha_{\text{sc}} \right]^2 + \left[ \frac{\Omega_{\odot}}{V_{\text{sw}}} \delta V_{\text{sw}} \right]^2}, \quad (19)$$

with  $\delta V_{\text{sw}}$  the uncertainty in the solar-wind speed estimate, and  $\delta\beta_{\text{tra}}$  accounts for interplanetary transport effects ignored by the model. Similarly, the error on the footpoint latitude takes into account the deviations from the spiral-model approximation out of the equatorial plane and effects related to the differential changes across the solar surface.

## References

- Adriani, O., Barbarino, G.C., Bazilevskaya, G.A., Bellotti, R., Boezio, M., Bogomolov, E.A., Bongi, M., Bonvicini, V., Bottai, S., Bruno, A., Cafagna, F., Campana, D., Carlson, P., Casolino, M., Castellini, G., De Santis, C., Di Felice, V., Galper, A.M., Karelin, A.V., Koldashov, S.V., Koldobskiy, S., Krutkov, S.Y., Kvashnin, A.N., Leonov, A., Malakhov, V., Marcelli, L., Martucci, M., Mayorov, A.G., Menn, W., Mergè, M., Mikhailov, V.V., Mocchiutti, E., Monaco, A., Munini, R., Mori, N., Osteria, G., Panico, B., Papini, P., Pearce, M., Picozza, P., Ricci, M., Ricciarini, S.B., Simon, M., Sparvoli, R., Spillantini, P., Stozhkov, Y.I., Vacchi, A., Vannuccini, E., Vasilyev, G., Voronov, S.A., Yurkin, Y.T., Zampa, G., Zampa, N.: 2017, Ten years of PAMELA in space. *La Rivista del Nuovo Cimento* **40**, 473. [DOI](#).
- Bruno, A.: 2017, Calibration of the GOES 13/15 high-energy proton detectors based on the PAMELA solar energetic particle observations. *Space Weather* **15**, 1191. [DOI](#).
- Bruno, A., Bazilevskaya, G.A., Boezio, M., Christian, E.R., de Nolfo, G.A., Martucci, M., Mergè, M., Mikhailov, V.V., Munini, R., Richardson, I.G., Ryan, J.M., Stochaj, S., Adriani, O., Barbarino, G.C., Bellotti, R., Bogomolov, E.A., Bongi, M., Bonvicini, V., Bottai, S., Cafagna, F., Campana, D., Carlson, P., Casolino, M., Castellini, G., Santis, C.D., Felice, V.D., Galper, A.M., Karelin, A.V., Koldashov, S.V., Koldobskiy, S., Krutkov, S.Y., Kvashnin, A.N., Leonov, A., Malakhov, V., Marcelli, L., Mayorov, A.G., Menn, W., Mocchiutti, E., Monaco, A., Mori, N., Osteria, G., Panico, B., Papini, P., Pearce, M., Picozza, P., Ricci, M., Ricciarini, S.B., Simon, M., Sparvoli, R., Spillantini, P., Stozhkov, Y.I., Vacchi, A., Vannuccini, E., Vasilyev, G.I., Voronov, S.A., Yurkin, Y.T., Zampa, G., Zampa, N.: 2018, Solar energetic particle events observed by the PAMELA mission. *Astrophys. J.* **862**, 97. [DOI](#).
- Bruno, A., Christian, E.R., de Nolfo, G.A., Richardson, I.G., Ryan, J.M.: 2019, Spectral analysis of the September 2017 solar energetic particle events. *Space Weather* **17**. [DOI](#).
- Cane, H.V., Reames, D.V., von Rosenvinge, T.T.: 1988, The role of interplanetary shocks in the longitude distribution of solar energetic particles. *J. Geophys. Res.* **93**, 9555. [DOI](#).
- Cane, H.V., Richardson, I.G., von Rosenvinge, T.T.: 2010, A study of solar energetic particle events of 1997–2006: Their composition and associations. *J. Geophys. Res.* **115**, A08101. [DOI](#).
- Caprioli, D., Spitkovsky, A.: 2014, Simulations of ion acceleration at non-relativistic shocks. I. Acceleration efficiency. *Astrophys. J.* **783**, 91. [DOI](#).

- Cliiver, E.W.: 2006, The unusual relativistic solar proton events of 1979 August 21 and 1981 May 10. *Astrophys. J.* **639**, 1206. DOI.
- Cohen, C.M.S., Mason, G.M., Mewaldt, R.A.: 2017, Characteristics of solar energetic ions as a function of longitude. *Astrophys. J.* **843**, 132. DOI.
- Cucinotta, F.A., Hu, S., Schwadron, N.A., Kozarev, K., Townsend, L.W., Kim, M.-H.Y.: 2010, Space radiation risk limits and Earth-Moon-Mars environmental models. *Space Weather* **8**, S00E09. DOI.
- Dalla, S., Agueda, N.: 2010, Role of latitude of source region in solar energetic particle events. In: Maksimovic, M., Meyer-Vernet, N., Moncuquet, M., Pantellini, F. (eds.) *20th Internat. Solar Wind Conf.* CP-1216, American Institute of Physics, Melville, 613. DOI.
- Dalla, S., Marsh, M.S., Battarbee, M.: 2017, Solar energetic particle drifts and the energy dependence of 1 au charge states. *Astrophys. J.* **834**, 167. DOI.
- Dalla, S., Marsh, M.S., Kelly, J., Laitinen, T.: 2013, Solar energetic particle drifts in the Parker spiral. *J. Geophys. Res.: Space Physics* **118**, 5979. DOI.
- de Nolfo, G.A., Bruno, A., Ryan, J.M., Dalla, S., Giacalone, J., Richardson, I.G., Christian, E.R., Stochaj, S.J., Bazilevskaya, G.A., Boezio, M., Martucci, M., Mikhailov, V.V., Munini, R.: 2019, Comparing long-duration gamma-ray flares and high-energy solar energetic particles. *Astrophys. J.* **879**, 90. DOI.
- Desai, M.I., Giacalone, J.: 2016, Large gradual solar energetic particle events. *Liv. Rev. in Solar Phys.* **13**, 3. DOI.
- Desai, M.I., Mason, G.M., Gold, R.E., Krimigis, S.M., Cohen, C.M.S., Mewaldt, R.A., Mazur, J.E., Dwyer, J.R.: 2006, Heavy-ion elemental abundances in large solar energetic particle events and their implications for the seed population. *Astrophys. J.* **649**, 470. DOI.
- Desai, M.I., Mason, G.M., Dayeh, M.A., Ebert, R.W., Mccomas, D.J., Li, G., Cohen, C.M.S., Mewaldt, R.A., Schwadron, N.A., Smith, C.W.: 2016, Spectral properties of large gradual solar energetic particle events. I. Fe, O, and seed material. *Astrophys. J.* **816**, 68. DOI.
- Ding, L., Jiang, Y., Zhao, L., Li, G.: 2013, The “twin-CME” scenario and large solar energetic particle events in solar cycle 23. *Astrophys. J.* **763**, 30. DOI.
- Eastwood, J.P., Biffis, E., Hapgood, M.A., Green, L., Bisi, M.M., Bentley, R.D., Wicks, R., McKinnell, L.-A., Gibbs, M., Burnett, C.: 2017, The economic impact of space weather: Where do we stand? *Risk Analysis* **37**, 206. DOI.
- Ellison, D.C., Ramaty, R.: 1985, Shock acceleration of electrons and ions in solar flares. *Astrophys. J.* **298**, 400. DOI.
- Giacalone, J., Jokipii, J.R.: 2012, The longitudinal transport of energetic ions from impulsive solar flares in interplanetary space. *Astrophys. J. Lett.* **751**, 33. DOI.
- Gopalswamy, N., Mäkelä, P.: 2014, Latitudinal Connectivity of Ground Level Enhancement Events. In: Hu, Q., Zank, G.P. (eds.) *Outstanding Problems in Heliophysics: From Coronal Heating to the Edge of the Heliosphere* CS-484, Astron. Soc. Pacific, San Francisco, 63. ADS.
- Gopalswamy, N., Yashiro, S., Krucker, S.: 2004, Intensity variation of large solar energetic particle events associated with coronal mass ejections. *J. Geophys. Res.* **109**, A12105. DOI.
- Gopalswamy, N., Yashiro, S., Michalek, G., Kaiser, M.L., Howard, R.A., Reames, D.V., Leske, R., von Rosenvinge, T.: 2002, Interacting coronal mass ejections and solar energetic particles. *Astrophys. J. Lett.* **572**, 103. DOI.
- Gopalswamy, N., Xie, H., Yashiro, S., Usoskin, I.: 2005, Coronal Mass Ejections and Ground Level Enhancements. In: Acharya, B.S., Gupta, S., Jagadeesan, P., Jain, A., Karthikeyan, S., Morris, S., Tonwar, S. (eds.) *Proc. 29th Internat. Cosmic Ray Conf., Internat. Cosmic Ray Conf.* **1**, Tata Institute of Fundamental Research, Mumbai, 169. ADS.
- Gopalswamy, N., Xie, H., Akiyama, S., Yashiro, S., Usoskin, I.G., Davila, J.M.: 2013, The first ground level enhancement event of solar cycle 24: Direct observation of shock formation and particle release heights. *Astrophys. J. Lett.* **765**, 30. DOI.
- Gopalswamy, N., Xie, H., Akiyama, S., Mäkelä, P.A., Yashiro, S.: 2014, Major solar eruptions and high-energy particle events during solar cycle 24. *Earth, Planets and Space* **66**, 104. DOI.
- Ippolito, A., Pommois, P., Zimbardo, G., Veltri, P.: 2005, Magnetic connection from the Earth to the solar corona, flare positions and solar energetic particle observations. *Astron. Astrophys.* **438**, 705. DOI.
- Jokipii, J.R.: 1966, Cosmic-Ray Propagation. I. Charged Particles in a Random Magnetic Field. *Astrophys. J.* **146**, 480. DOI. ADS.

- Kahler, S.W.: 2001, The correlation between solar energetic particle peak intensities and speeds of coronal mass ejections: Effects of ambient particle intensities and energy spectra. *J. Geophys. Res.* **106**, 20947. DOI.
- Kahler, S.W., Vourlidas, A.: 2005, Fast coronal mass ejection environments and the production of solar energetic particle events. *J. Geophys. Res.* **110**, A12S01. DOI.
- Kahler, S.W., Hildner, E., Van Hollebeke, M.A.I.: 1978, Prompt solar proton events and coronal mass ejections. *Solar Phys.* **57**, 429. DOI.
- Kahler, S.W., Reames, D.V., Burkepile, J.T.: 2000, A Role for Ambient Energetic Particle Intensities in Shock Acceleration of Solar Energetic Particles. In: Ramaty, R., Mandzhavidze, N. (eds.) *High Energy Solar Phys. Workshop - Anticipating HESSI CS-206*, Astronom. Soc. Pacific, San Francisco, 468. ADS.
- Kahler, S.W., Sheeley Jr., N.R., Howard, R.A., Koomen, M.J., Michels, D.J., McGuire, R.E., von Roseninge, T.T., Reames, D.V.: 1984, Associations between coronal mass ejections and solar energetic proton events. *J. Geophys. Res.: Space Physics* **89**, 9683. DOI.
- Kahler, S.W., Cliver, E.W., Cane, H.V., McGuire, R.E., Reames, D.V., Sheeley Jr., N.R., Howard, R.A.: 1987, Solar Energetic Proton Events and Coronal Mass Ejections Near Solar Minimum. In: Kozyarivsky, V.A., Lidvanskij, A.S., Tulupova, T.I., Tsyabuk, A.L., Voevodskij, A.V., Volgmut, N.S. (eds.) *Proc. 20th Internat. Cosmic Ray Conf., Internat. Cosmic Ray Conf.* **3**, Nauka, Moscow, 121. ADS.
- Kaiser, M.L., Kucera, T.A., Davila, J.M., St. Cyr, O.C., Guhathakurta, M., Christian, E.: 2008, The STEREO mission: An introduction. *Space Sci. Rev.* **136**, 5. DOI.
- Kallenrode, M.-B.: 1993, Neutral lines and azimuthal transport of solar energetic particles. *J. Geophys. Res.: Space Physics* **98**, 5573. DOI.
- Kong, X., Guo, F., Giacalone, J., Li, H., Chen, Y.: 2017, The acceleration of high-energy protons at coronal shocks: The effect of large-scale streamer-like magnetic field structures. *Astrophys. J.* **851**, 38. DOI.
- Kong, X., Guo, F., Chen, Y., Giacalone, J.: 2019, The acceleration of energetic particles at coronal shocks and emergence of a double power-law feature in particle energy spectra. *Astrophys. J.* **883**, 49. DOI.
- Laitinen, T., Kopp, A., Effenberger, F., Dalla, S., Marsh, M.S.: 2016, Solar energetic particle access to distant longitudes through turbulent field-line meandering. *Astron. Astrophys.* **591**, A18. DOI.
- Lario, D., Karelitz, A.: 2014, Influence of interplanetary coronal mass ejections on the peak intensity of solar energetic particle events. *J. Geophys. Res.: Space Physics* **119**, 4185. DOI.
- Lario, D., Roelof, E.C., Decker, R.B.: 2014, Longitudinal Dependence of SEP Peak Intensities as Evidence of CME-Driven Shock Particle Acceleration. In: Hu, Q., Zank, G.P. (eds.) *Outstanding Problems in Heliophysics: From Coronal Heating to the Edge of the Heliosphere CS-484*, Astron. Soc. Pacific, San Francisco, 98. ADS.
- Lario, D., Kallenrode, M.-B., Decker, R.B., Roelof, E.C., Krimigis, S.M., Aran, A., Sanahuja, B.: 2006, Radial and longitudinal dependence of solar 4–13 MeV and 27–37 MeV proton peak intensities and fluences: Helios and IMP 8 observations. *Astrophys. J.* **653**, 1531. DOI.
- Lario, D., Aran, A., Gómez-Herrero, R., Dresing, N., Heber, B., Ho, G.C., Decker, R.B., Roelof, E.C.: 2013, Longitudinal And Radial Dependence Of Solar Energetic Particle Peak Intensities: STEREO, ACE, SOHO, GOES, And Messenger Observations. *Astrophys. J.* **767**, 41. DOI.
- Lee, C.O., Luhmann, J.G., Hoeksema, J.T., Sun, X., Arge, C.N., de Pater, I.: 2011, Coronal field opens at lower height during the solar cycles 22 and 23 minimum periods: IMF comparison suggests the source surface should be lowered. *Solar Phys.* **269**, 367. DOI.
- Lee, M.A.: 2005, Coupled hydromagnetic wave excitation and ion acceleration at an evolving coronal/interplanetary shock. *Astrophys. J. Suppl.* **158**, 38. DOI.
- Li, G., Moore, R., Mewaldt, R.A., Zhao, L., Labrador, A.W.: 2012, A twin-CME scenario for ground level enhancement events. *Space Sci. Rev.* **171**, 141. DOI.
- Liu, Y., Davies, J.A., Luhmann, J.G., Vourlidas, A., Bale, S.D., Lin, R.P.: 2010, Geometric Triangulation Of Imaging Observations To Track Coronal Mass Ejections Continuously Out To 1 AU. *Astrophys. J. Lett.* **710**, 82. DOI.
- Masson, S., Démoulin, P., Dasso, S., Klein, K.-L.: 2012, The interplanetary magnetic structure that guides solar relativistic particles. *Astron. Astrophys.* **538**, A32. DOI.
- Mays, M.L., Taktakishvili, A., Pulkkinen, A., MacNeice, P.J., Rastätter, L., Odstrcil, D., Jian, L.K., Richardson, I.G., LaSota, J.A., Zheng, Y., Kuznetsova, M.M.: 2015, Ensemble modeling of CMEs using the WSA-ENLIL+Cone model. *Solar Phys.* **290**, 1775. DOI.

- Mewaldt, R.A., Cohen, C.M.S., Cook, W.R., Cummings, A.C., Davis, A.J., Geier, S., Kecman, B., Klemic, J., Labrador, A.W., Leske, R.A., Miyasaka, H., Nguyen, V., Ogliore, R.C., Stone, E.C., Radocinski, R.G., Wiedenbeck, M.E., Hawk, J., Shuman, S., von Roseninge, T.T., Wortman, K.: 2008, The Low-Energy Telescope (LET) and SEP central electronics for the STEREO mission. *Space Sci. Rev.* **136**, 285. DOI.
- Müller-Mellin, R., Böttcher, S., Falenski, J., Rode, E., Duvet, L., Sanderson, T., Butler, B., Johlander, B., Smit, H.: 2008, The solar electron and proton telescope for the STEREO mission. *Space Sci. Rev.* **136**, 363. DOI.
- Onsager, T., Grubb, R., Kunches, J., Matheson, L., Speich, D., Zwickl, R.W., Sauer, H.: 1996, Operational uses of the GOES energetic particle detectors. In: Washwell, E.R. (ed.) *GOES-8 and Beyond, Proc. Internat. Soc. for Optics and Photo. (SPIE)* **2812**, 281. DOI.
- Paasilta, M., Papaioannou, A., Dresing, N., Vainio, R., Valtonen, E., Heber, B.: 2018, Catalogue of >55 MeV wide-longitude solar proton events observed by SOHO, ACE, and the STEREOs at  $\approx 1$  AU during 2009–2016. *Solar Phys.* **293**, 70. DOI.
- Parker, E.N.: 1958, Dynamics of the interplanetary gas and magnetic fields. *Astrophys. J.* **128**, 664. DOI.
- Posner, A.: 2007, Up to 1-hour forecasting of radiation hazards from solar energetic ion events with relativistic electrons. *Space Weather* **5**. DOI.
- Posner, A., Heber, B., Rother, O., Guetersloh, S.: 2009, A new trend in forecasting solar radiation hazards. *Space Weather* **7**, S05001. DOI.
- Reames, D.V.: 2000, Particle acceleration by CME-driven shock waves. In: Kieda, D.B., Salamon, M.B., Dingus, B.L. (eds.) *Proc. 26th Internat. Cosmic Ray Conf.* **516**, American Institute of Physics, Salt Lake City, 289.
- Reames, D.V.: 2009, Solar energetic-particle release times in historic ground-level events. *Astrophys. J.* **706**, 844. DOI.
- Richardson, I.G., Mays, M.L., Thompson, B.J.: 2018, Prediction of solar energetic particle event peak proton intensity using a simple algorithm based on CME speed and direction and observations of associated solar phenomena. *Space Weather* **16**, 1862. DOI.
- Richardson, I.G., von Roseninge, T.T., Cane, H.V.: 2015, The properties of solar energetic particle event-associated coronal mass ejections reported in different CME catalogs. *Solar Phys.* **290**, 1741. DOI.
- Richardson, I.G., von Roseninge, T.T., Cane, H.V.: 2017, 25 MeV solar proton events in cycle 24 and previous cycles. *Adv. in Space Res.* **60**, 755. Solar Energetic Particles, Solar Modulation and Space Radiation: New Opportunities in the AMS-02 Era. DOI.
- Richardson, I.G., von Roseninge, T.T., Cane, H.V., Christian, E.R., Cohen, C.M.S., Labrador, A.W., Leske, R.A., Mewaldt, R.A., Wiedenbeck, M.E., Stone, E.C.: 2014, > 25 mev proton events observed by the high energy telescopes on the stereo a and b spacecraft and/or at earth during the first  $\sim$ seven years of the stereo mission. *Solar Phys.* **289**, 3059. DOI.
- Sandberg, I., Jiggins, P., Heynderickx, D., Daglis, I.A.: 2014, Cross calibration of NOAA GOES solar proton detectors using corrected NASA IMP-8/GME data. *Geophysical Research Letters* **41**, 4435. DOI.
- Sanderson, R.T., Beeck, J., Marsden, G.R., Tranquille, C., Wenzel, K.-P., McKibben, B.R., Smith, J.E.: 1990, Cosmic Ray, Energetic Ion and Magnetic Field Characteristics of a Magnetic Cloud. In: Protheroe, R.J. (ed.) *Proc. 21st Internat. Cosmic Ray Conf., International Cosmic Ray Conference* **6**, University of Adelaide, Adelaide, 255. ADS.
- Shea, M.A., Smart, D.F.: 2012, Space weather and the ground-level solar proton events of the 23rd solar cycle. *Space Sci. Rev.* **171**, 161. DOI.
- Snodgrass, H.B., Ulrich, R.K.: 1990, Rotation of Doppler Features in the Solar Photosphere. *Astrophys. J.* **351**, 309. DOI. ADS.
- St. Cyr, O.C., Posner, A., Burkepile, J.T.: 2017, Solar energetic particle warnings from a coronagraph. *Space Weather* **15**, 240. DOI.
- Struminsky, A., Heber, B., Kallenrode, M.-B., Müller-Mellin, R., Klassen, A., Kunow, H.: 2006, Injection and propagation of solar protons to high heliospheric latitudes: Ulysses Ket observations. *Adv. in Space Res.* **38**, 507. Coronal Mass Ejections and Solar Particle Events in Solar Cycle 23. DOI.
- Tylka, A.J., Cohen, C.M.S., Dietrich, W.F., Lee, M.A., MacLennan, C.G., Mewaldt, R.A., Ng, C.K., Reames, D.V.: 2005, Shock geometry, seed populations, and the origin of variable elemental composition at high energies in large gradual solar particle events. *Astrophys. J.* **625**, 474. DOI.
- Van Hollebeke, M.A.I., Ma Sung, L.S., McDonald, F.B.: 1975, The variation of solar proton energy spectra and size distribution with heliolongitude. *Solar Phys.* **41**, 189. DOI.

- von Rosenvinge, T.T., Reames, D.V., Baker, R., Hawk, J., Nolan, J.T., Ryan, L., Shuman, S., Wortman, K.A., Mewaldt, R.A., Cummings, A.C., Cook, W.R., Labrador, A.W., Leske, R.A., Wiedenbeck, M.E.: 2008, The High Energy Telescope for STEREO. *Space Sci. Rev.* **136**, 391. [DOI](#).
- Zank, G.P., Li, G., Verkhoglyadova, O.: 2007, Particle acceleration at interplanetary shocks. *Space Sci. Rev.* **130**, 255. [DOI](#).
- Zhao, L., Li, G.: 2014, Particle acceleration at a pair of parallel shocks near the Sun. *J. Geophys. Res.: Space Physics* **119**, 6106. [DOI](#).
- Zhao, L., Zhang, M., Rassoul, H.K.: 2016, Double power laws in the event-integrated solar energetic particle spectrum. *Astrophys. J.* **821**, 62. [DOI](#).